2 THEORETICAL BASICS AND DEVELOPMENT OF THE ANALYTICAL SOLUTION

In the previous Chapter 1.1 the concept of isostasy was explained. The Airy and Pratt model of isostasy assume that the topography is locally compensated. The most important assumption of the Vening-Meinesz Model is that the lithosphere behaves as a perfectly elastic material. That is why his flexure model is called elastic plate model. Because of the disadvantage of the spectral methods (Chapter 1.2.) I aim to find an analytical solution. In order to provide an analytical solution, it is essential to understand the theory of the elastic plate model. Therefore I will investigate the assumptions behind the elastic plate model and the history of the differential equation of the 4th order, which describes the flexure of an elastic plate.

2.1 DIFFERENTIAL EQUATION

2.1.1 Plate Theory According To Kirchhoff

In the plate theory the following assumptions are made:

1. the dimension of the plate (x, y direction) is large compared to the dimension in z direction
2. T_e corresponds to the thickness of the plate
3. the load is acting vertical to the middle plane of the plate in the z direction
4. the temperature distribution could cause deformation and tension (this is expressed by the moment of temperature)

The differential equation for the elastic plate model is called thin plate approximation, according to assumption no. 1., which leads to an error discussed in Chapter 4.1. The middle plane of the plate is called neutral surface (Fig. 2.1.1). The reason is, that if a plate is deflected, then in the upper part occurs compression and in the lower part extension. The middle part is the part of no tension.

Figure 2.1.1) The upper part of an elastic plate is compressed and the lower part extended. In the middle plane occurs no tension, therefore this plane is called neutral surface.

The flexure of an elastic plate has been a subject of investigation by mechanical engineers (e.g. GÖLDNER 1978, GÖLDNER 1988, TIMOSHENKO & WOINOWSKI-KRIEGER 1959, HETÉNYI 1979). The origin I find in the plate theory developed by the physicist G. R. Kirchhoff (1824-1887). For small deflections the flexure of an elastic plate is explicate by a differential equation with:

$$\Delta\Delta w = \frac{1}{D}\left(p - \frac{\Delta m_\Theta}{1-\nu}\right) \qquad \textbf{(2.1.1)}$$

with $p = f(x, y)$ as force per unit area, D as flexural rigidity and Δ as Laplace operator, which can be written in Cartesian coordinates: $\Delta = \frac{\partial^2}{\partial x^2} + \frac{\partial^2}{\partial y^2}$. Furthermore is m_Θ the moment of temperature:

$$m_\Theta = \alpha E \cdot \int_{-\frac{T_e}{2}}^{\frac{T_e}{2}} \Theta \cdot z \cdot dz \qquad \textbf{(2.1.2)}$$

$\alpha\left[K^{-1}\right]$ is the coefficient of thermal expansion and Θ is the temperature difference (GÖLDNER 1978). In the following investigation the temperature is not considered. However, a discussion about the moment of temperature follows in Chapter 4.2 .

The differential equation was modified for the deformation of a beam that overlie an elastic foundation. This was based on the assumption that the reaction forces of the foundation are proportional at every point to the deflection of the beam at that point. This assumption was first introduced by E. Winkler (WINKLER 1867) and formed the basis of H. Zimmermann's classical work on the railroad track in Berlin (ZIMMERMANN 1888).

The most debated part of Winkler's assumption: that the foundation deforms only along the portion directly under loading, has often been found to be true since FÖPPEL's classical experiment (FÖPPEL 1922). In the following a more simple form of the differential equation after HETÉNYI (1979) will be investigated.

2.1.2 Beam on elastic foundation

A beam is considered, which is supported along its entire length by an elastic medium and subjected to vertical forces acting in the principal plane of the symmetrical cross section (Fig. 2.1.2). Because of this action the beam will deflect, producing continuously distributed reaction forces in the supporting medium. Regarding this reaction forces a fundamental assumption is made. The intensity of the reaction force F at any point is proportional to the deflection w at that point:

$$F = k \cdot w \qquad \textbf{(2.1.3)}$$

with $k = const$ as factor. This assumption implies the statement that the supporting medium is elastic; and the process can be described through the Hook's law. The reaction forces will be assumed to be acting vertically and opposing the deflection of the beam.

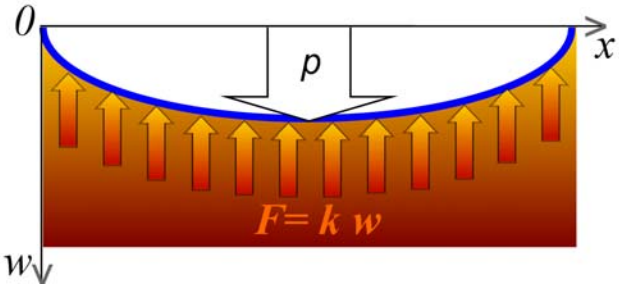

Figure 2.1.2) The differential equation of the elastic line takes the restoring force of the foundation into account. The deflection w is considered in one dimension x.

While the loaded beam deflects, it is possible that besides the vertical reactions there may also be some horizontal (frictional) forces originating along the interface between the beam and the foundation. Their effect is assumed to be very small and will not be considered. In the next step an infinitely small element from side length dx is considered.

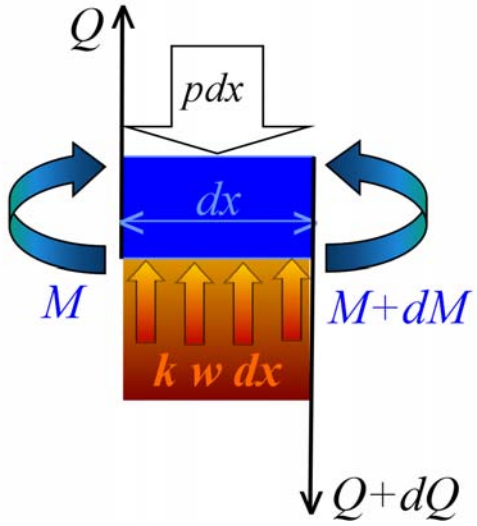

Figure 2.1.3) Description for flexure of the elastic line in a portion dx. Shown is direction of shearing force Q and corresponding bending moment M.

The Fig. 2.1.3 shows the forces, which are exerted on such element. The upward acting shearing force Q is considered positive, like the corresponding bending moment M. If I consider the equilibrium of forces, follows with summation of the vertical forces:

$$Q - (Q + dQ) + kwdx - pdx = 0 \qquad \textbf{(2.1.4)}$$

therefore:

$$\frac{dQ}{dx} = kw - p \qquad \textbf{(2.1.5)}$$

The bending moment M and the shearing force Q are related through (HETÉNYI 1979):

$$dM = Q \cdot dx \qquad \textbf{(2.1.6)}$$

With use of this relation the Eq. 2.1.5 leads to:

$$\frac{d^2M}{dx^2} = kw - p \qquad \textbf{(2.1.7)}$$

The differential equation for a bending beam is:

$$EI\frac{d^2w}{dx^2} = -M \qquad \textbf{(2.1.8)}$$

with I as moment of inertia and E as Young's modulus. For a beam with side length a and thickness T_e is the moment of inertia (BORN 1968, ISSLER ET AL. 1995):

$$I = \frac{aT_e^{\,3}}{12(1-\nu^2)} \qquad \textbf{(2.1.9)}$$

The factor $E \cdot I$ corresponds to D. Therefore it can be written (HETÉNYI 1979):

$$D\frac{d^2w}{dx^2} = -M \qquad \textbf{(2.1.10)}$$

If I differentiate Eq. 2.1.10 twice, I obtain:

$$D\frac{d^4w}{dx^4} = -\frac{d^2M}{dx^2} \qquad \textbf{(2.1.11)}$$

the Eq. 2.1.7 leads to:

$$D\frac{d^4w}{dx^4} = -kw + p \qquad \textbf{(2.1.12)}$$

By comparison of the differential Eq. 2.1.12 with Eq. 2.1.1 it is obviously that the temperature moment is not regarded. However, an additional term is considered, which describes the reaction force as a consequence of the elastic foundation.

2.1.3 Application in geological sciences

The differential Eq. (2.1.12) for a beam was extended for a problem to an elastic plate. The restoring force in the Earth can be described through the density contrast; consequently the proportional factor k is replaced (e.g. TURCOTTE & SCHUBERT 1982) with:

$$(\rho_m - \rho_c)g = k \qquad \textbf{(2.1.13)}$$

In the geological science usually the scientists concern loads of a certain shape that act on the surface and the base of the crust. It is therefore more convenient to replace the forces F per unit area A by a load of a specified height h and density, with V as volume follows:

$$p = \frac{F}{A} = \frac{mg}{A} = \frac{\rho Vg}{A} = \frac{\rho Vg}{Vh^{-1}} = \rho gh \qquad \textbf{(2.1.14)}$$

With use of Eq. 2.1.12, 2.1.13 and 2.1.14 the deflection w can be described with $\vec{r} = r(x, y)$ (e.g. TURCOTTE & SCHUBERT 1982):

$$\Delta\left[D(\vec{r})\Delta w(\vec{r})\right] + (\rho_m - \rho_c)gw(\vec{r}) = \rho_c gh \qquad \textbf{(2.1.15)}$$

thereby this equation is three dimensional. With use of Eq. 2.1.11 and 2.1.6 it is achieved:

$$D\frac{d^4 w}{d\vec{r}^{\,4}} = -\frac{dQ}{d\vec{r}} \qquad \textbf{(2.1.16)}$$

Considering the x direction the 4th derivation of the deflection w is related to a variation of the shearing force Q. According to Eq. 2.1.15 and 2.1.16 I can write:

$$-\frac{\partial Q}{\partial x} + (\rho_m - \rho_c)gw(x) = \rho_c gh \qquad \textbf{(2.1.17)}$$

Considering the Newton's law "actio = reactio", I can describe this differential equation with simple words (Fig. 2.1.4): the "actio" is the load = $\rho_c gh$; the resulting deflection produces continuously distributed reaction forces in the supporting medium. The "reactio" mathematically is described with $(\rho_m - \rho_c)gw(x)$, meaning that the restoring force is a result of the replacement of mantle material by crustal material. The intensity of this restoring force was assumed to be proportional to the deflection of the plate w (see Eq. 2.1.3).

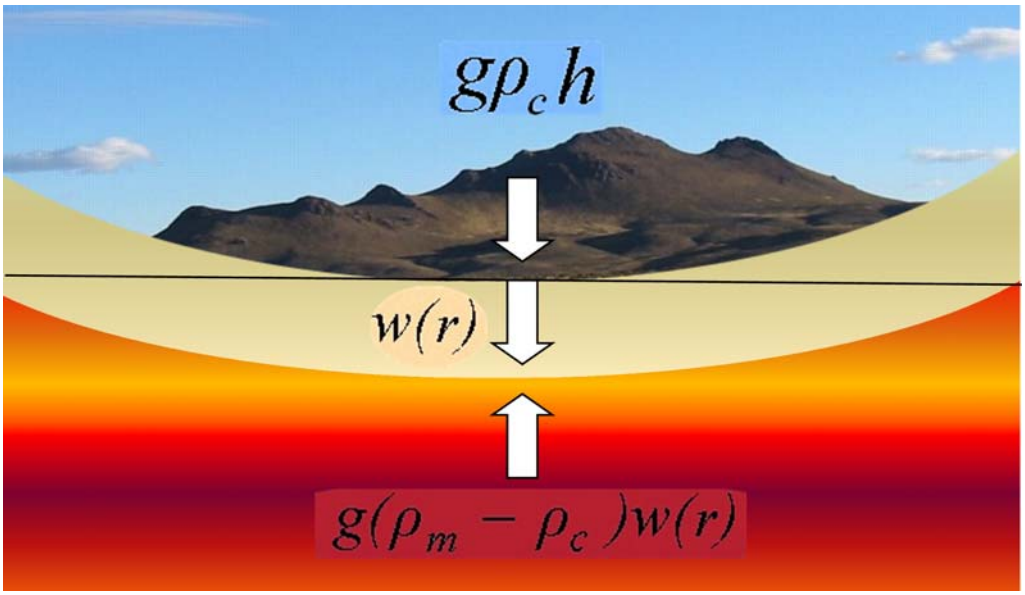

Figure 2.1.4) Description for the differential equation according to the Newton's principia of actio = reactio.

According to the concept of isostasy (VENING-MEINESZ 1939), the isostatic compensation is regional and controlled by the lithospheric plate (see Chapter 1.1.3). Additional to the vertical component a horizontal one has to be taken into account for the equilibrium of forces. This is mathematically illustrated through the variation of the shearing force $-\frac{\partial Q}{\partial x}$ describing the strength of the lithospheric plate. Thereby Eq. 2.1.16 proves that the greater the flexural rigidity of the plate the greater is the horizontal shearing force, therefore less is the deflection of the plate.

The differential Eq. 2.1.15 had until recently not been analytically solved for an irregularly shaped topography. One analytical solution for the differential equation was developed by HERTZ (1884) for a point load, without taking a elastic foundation and temperature moment into account. His formulas were used in order to derive a new analytical solution for the application in the geological sciences; therefore Hertz's solution will be introduced in the following chapter.

2.2 FORMULA ACCORDING TO HERTZ

In this chapter the formula developed by HERTZ (1884) will be investigated. The introduction of the formula is important in order to understand the analytic solution. Many preliminary investigations were necessary, because the analytic solution is not simply a use of an already existing formula. I will use three equations according to Hertz in order to obtain one analytical solution. The three so-called "Hertz's formulas" are solutions of the elastic plate equation in three dimensions. Hertz had applied it to the problem of the deformation of an ice sheet caused by a weight and not of a load. Therefore it is necessary to make the formulas applicable to geological sciences. This will lead to the analytical solution for the deflection of the elastic lithosphere due to a topographic load.

An infinitely expanded elastic plate (e.g. ice) floats on an infinitely extendend liquid (e.g. water), whereon weights are placed causing no lateral tension. Considering only small shifts the effect of the weights can be superimposed. For this reason it is sufficient to take only one weight P into account. The load of this weight concentrates on the origin of the coordinate system. The plane of the coordinate system is coincident with the $x-y$ plane of the thin flexible plate. Because the solution is radially symmetric, it is suitable to consider a radius, describable at the distance from the center:

$$\rho^2 = x^2 + y^2 \qquad \textbf{(2.2.1)}$$

Remark: The use of the symbol ρ for the radius is probably confusing since this symbol is the conventional notation of the density, but I want to write here the orginal symbols used by HERTZ (1884), in order to avoid confusions. In the following chapter (2.3) the usual symbols will be introduced. Given is z as the vertical deflection of the deformed plate from the $x-y$ plane. The weight P is acting on the origin of the coordinate system. Hertz considered the specific weight of the fluid s and the thickness of the plate h. For the elastic parameters of the plate he used the Young's modulus E and the Poisson's ratio μ. I will use in the following ν as notation for the Poisson's ratio. The elastic force $\frac{Eh^3}{12(1-\nu^2)}\Delta\cdot\Delta z$ is acting per unit area with focus to the top. Thereby Δ is the notation for the Laplace operator , with $\Delta = \frac{\partial^2}{\partial x^2} + \frac{\partial^2}{\partial y^2}$. The hydrostatic restoring force $s\cdot z$ is directed towards to the top. The sum of the two forces has to be zero except in the point of origin. It follows that

$$\frac{Eh^3}{12(1-\nu^2)}\Delta\cdot\Delta z + s\cdot z = 0 \qquad \textbf{(2.2.2);}$$

therefore

$$\Delta\cdot\Delta z + s\frac{12(1-\nu^2)}{Eh^3}z = 0 \qquad \textbf{(2.2.3)}$$

The integral-value of the sum calculated over a small surface must be equivalent to the weight in the point of origin of the coordinate system. But the integral-value of the hydrostatic pressure disappears over such a small surface. Therefore it is permissible to use the integral-value for the elastic reaction. Now I will use a shortcut:

$$a^4 = \frac{12(1-\nu^2)}{Eh^3}s \quad \text{with}: \; a^4 = \frac{1}{\alpha^4} \;\Rightarrow\; \alpha^4 = \frac{Eh^3}{12(1-\nu^2)} \cdot \frac{1}{s} \qquad \textbf{(2.2.4)}$$

thus gives for Eq. 2.2.3: $$\Delta \cdot \Delta z + a^4 z = 0 \qquad \textbf{(2.2.5)}$$

I found a mathematical description for the problem: An integral of the Eq. 2.2.5 has to be found, which disappears in the infinite, is finite in the origin point of the coordinate system and in the neighbourhood of the origin it should be equal to P. According to HEINE (1878) is:

$$K(\rho) = \int_0^\infty e^{i\rho \cos iu} du \qquad \textbf{(2.2.6)}$$

a solution of the differential equation $\Delta z + z = 0$ (with u as a variable of integral). It follows that $K(\rho \cdot \sqrt[4]{-a^4})$ is a solution of the Eq. 2.2.5. Therefore I can solve Eq. 2.2.5 with Eq. 2.2.6 and it results a solution in the imaginary number space:

$$z = \frac{a^2 P}{4\pi s \cdot i} \cdot \left\{ K\left[a\rho\sqrt{\frac{1}{2}} \cdot (1+i) \right] - K\left[a\rho\sqrt{\frac{1}{2}} \cdot (1-i) \right] \right\} \qquad \textbf{(2.2.7)}$$

However, this solution is real. Therefore it is transformed into a solution for the real part. This is inserted into Eq. 2.2.7 and it follows (HERTZ 1884):

$$z = \frac{a^2 P}{4\pi s} \cdot \int_1^\infty \frac{e^{-a\rho\sqrt{1/2}\xi} \sin a\rho\sqrt{1/2}\xi}{\sqrt{\xi^2 - 1}} d\xi \qquad \textbf{(2.2.8)}$$

with ξ as a variable of the integral. This form shows that the solution disappears in the infinity. For investigation of the values for the neighborhood (or vicinity) of the point of origin, the function K is expanded according to Bessel's functions and afterwards is it expanded in powers (potencies):

$$z = \frac{a^2 P}{2\pi s} \cdot \left\{ \begin{array}{l} \frac{a^2\rho^2}{2 \cdot 2} \cdot \log a\rho - \frac{a^6\rho^6}{2 \cdot 4 \cdot 6 \cdot 2 \cdot 4 \cdot 6} \cdot \left(\log a\rho - \frac{5}{6} \right) + \ldots \\ + \frac{\pi}{4} \left(1 - \frac{a^4\rho^4}{2 \cdot 4 \cdot 2 \cdot 4} + \frac{a^8\rho^8}{2 \cdot 4 \cdot 6 \cdot 8 \cdot 2 \cdot 4 \cdot 6 \cdot 8} - \ldots \right) \\ \ldots (1 + \log 2 - C) \cdot \left(\frac{a^2\rho^2}{2 \cdot 4} - \frac{a^6\rho^6}{2 \cdot 4 \cdot 6 \cdot 2 \cdot 4 \cdot 6} + \ldots \right) \end{array} \right\} \qquad \textbf{(2.2.9)}$$

with $C = 0.57721$. The series are arranged in such a way, that every horizontal-serie for itself represents a particular integral of the presented differential equation. It is suitable for the computation of small values of the radius ρ. The deflection z remains finite for $\rho = 0$ and reaches a finite value in the point of origin. This function (Eq. 2.2.9) is called "logarithm-function" in the following.
For greater values a semiconvergent series will be used, which is evolved from Eq. 2.2.8 by expansion after the radical and integration of the single elements. The first part is given as :

$$z = \frac{a^2 P}{2\pi s} \cdot \sqrt{\frac{\pi}{2}} \frac{e^{-a\rho\sqrt{\frac{1}{2}}}}{\sqrt{a\rho}} \left\{ \sin\left(a\rho\sqrt{\frac{1}{2}} + \frac{\pi}{8} \right) - \frac{1}{8\rho} \sin\left(a\rho\sqrt{\frac{1}{2}} + \frac{3\pi}{8} \right) + \ldots \right\} \qquad \textbf{(2.2.10)}$$

In the following this function is called "sine function". Hertz developed a solution valid at the point of the origin, where the plate reaches the maximal value of deflection.

$$z = z_0 = \frac{a^2 P}{8s} \qquad \textbf{(2.2.11)}$$

This investigation leads to three questions:

1.Which logarithm did Hertz use (base e, base 10)?
2.Which is the meaning of greater values of the radius?
3. How can a close and a wide range mathematically be descriped?

In order to find an answer, some examples proposed by HERTZ (1884) will be recalculated in the following chapters.

2.2.1 Investigation of the logarithm function

I will investigate the Eq. 2.2.9 for the logarithm function. It is questionable to which basis the logarithm corresponds. The denotation „log" means either the natural logarithm to the basis e (Euler number) or the logarithm to the basis 10. An example is given in the article of Hertz (1884, page 453). He calculated the following term:

$$\frac{a^4 P}{2\pi s} \left\{ \log aR - \frac{1}{2} - \log 2 + C \right\} = \frac{a^4 P}{2\pi s} \left\{ \log aR - 0.6519 \right\} \qquad \textbf{(2.2.12)}$$

with $C = 0.57721$. This example will be used to investigate which logarithm Hertz has used.

It follows: $$\left\{ -\frac{1}{2} - \log 2 + 0.57721 \right\} = \left\{ -0.6519 \right\} \qquad \textbf{(2.2.13)}$$

Calculation with "log" to the base of 10 gives:

$$\left\{ -\frac{1}{2} - \log 2 + C \right\} = \left\{ -0.2238 \right\} \qquad \textbf{(2.2.14)}$$

If I assume for "log" the logarithm to the base of e (natural logarithm), then I obtain:

$$\left\{-\frac{1}{2}-\ln 2+C\right\}=\left\{-0.6159\right\} \qquad \textbf{(2.2.15)}$$

The result of Eq. 2.2.15 is not the same value as in the article (Eq. 2.2.13); Hertz submitted as result $=\left\{-0.6519\right\}$. A possible reason might result from a typing error (interchange of cipher 1 with cipher 5). However, obviousily the denotation of Hertz means the natural logarithm. Because I want to use the convention for the present time, in the following I write "ln" instead of "log". For further investigation of the formula the distance (radius ρ) is calculated as a function from the parameter α. The results will be compared with the results proposed by HERTZ (1884, page 452).

radius ρ	z/z_0 calculated according to Hertz
α	0.646
$2\cdot\alpha$	0.258
$3\cdot\alpha$	0.66

Table 2.2.1) The ratio z/z_0 was calculated for different values for the radius ρ.

When using the radius $\rho=\alpha$ with Eq. 2.2.9, the following is obtained :

$$\frac{z}{z_0}=\frac{4}{\pi}\cdot\left\{\begin{array}{l}\dfrac{1}{2\cdot4\cdot6\cdot2\cdot4\cdot6}\cdot\left(\dfrac{5}{6}\right)+\ldots\\ +\dfrac{\pi}{4}\left(1-\dfrac{1}{2\cdot4\cdot2\cdot4}+\dfrac{1}{2\cdot4\cdot6\cdot8\cdot2\cdot4\cdot6\cdot8}-\ldots\right)\\ \ldots(1.1159)\cdot\left(\dfrac{1}{2\cdot2}-\dfrac{1}{2\cdot4\cdot6\cdot2\cdot4\cdot6}+\ldots\right)\end{array}\right\}=0.646 \qquad \textbf{(2.2.16)}$$

on condition that the 2nd and 3rd term of the sum within the product with $\frac{\pi}{4}$ is neglected. If I insert $\rho=2\cdot\alpha$ in Eq. 2.3.9, then follows:

$$\frac{z}{z_0}=\frac{4}{\pi}\cdot\left\{\begin{array}{l}\ln 2-\dfrac{2^6}{2\cdot4\cdot6\cdot2\cdot4\cdot6}\cdot\left(\ln 2-\dfrac{5}{6}\right)+\ldots\\ +\dfrac{\pi}{4}\left(1-\dfrac{2^4}{2\cdot4\cdot2\cdot4}+\dfrac{2^8}{2\cdot4\cdot6\cdot8\cdot2\cdot4\cdot6\cdot8}-\ldots\right)\\ \ldots(1.1159)\cdot\left(1-\dfrac{2^6}{2\cdot4\cdot6\cdot2\cdot4\cdot6}+\ldots\right)\end{array}\right\}=0.505 \qquad \textbf{(2.2.17)}$$

This is the not same value as given by Hertz. For $\rho=3\cdot\alpha$ I obtain:

$$\frac{z}{z_0}=\frac{4}{\pi}\cdot\left\{\begin{array}{l}\frac{3^2}{2^2}\ln 3-\frac{3^6}{2\cdot4\cdot6\cdot2\cdot4\cdot6}\cdot\left(\ln 3-\frac{5}{6}\right)+\ldots\\+\frac{\pi}{4}\left(1-\frac{3^4}{2\cdot4\cdot2\cdot4}+\frac{3^8}{2\cdot4\cdot6\cdot8\cdot2\cdot4\cdot6\cdot8}-\ldots\right)\\\ldots(1.1159)\cdot\left(\frac{3^2}{2^2}-\frac{3^6}{2\cdot4\cdot6\cdot2\cdot4\cdot6}+\ldots\right)\end{array}\right\}=0.072 \qquad \textbf{(2.2.18)}$$

which is not equivalent to the result proposed by Hertz, either (see Table 2.2.1). Therefore I assume that the logarithm function describes the neighborhood of the area of origin, where the point-load is acting. I will come back to this point later in the discussion (see Chapter 2.2.3).

2.2.2 Investigation of the sine function

Now I will investigate the Eq. 2.2.10.

I suspect a typing error in the puplished article, instead of $\frac{1}{8\rho}$ I use $\frac{1}{8\alpha\rho}$ (see orginal formula (4), HERTZ 1884, page 451). I modified the formula by replacing $term=\left\{-\frac{1}{8\rho}\sin\left(a\rho\sqrt{\frac{1}{2}}+\frac{3\pi}{8}\right)\right\}$ with $term=\left\{-\frac{1}{8a\rho}\sin\left(a\rho\sqrt{\frac{1}{2}}+\frac{3\pi}{8}\right)\right\}$. The distance can be calculated with the original formula (HERTZ 1884); for radius $\rho=\alpha$ is obtained:

$$\frac{z}{z_0}=\frac{4}{\pi}\cdot\sqrt{\frac{\pi}{2}}\frac{e^{-1\sqrt{\frac{1}{2}}}}{\sqrt{1}}\left\{\sin\left(\sqrt{\frac{1}{2}}+\frac{\pi}{8}\right)-\frac{1}{8\cdot\alpha}\sin\left(\sqrt{\frac{1}{2}}+\frac{3\pi}{8}\right)\right\}=0.701 \qquad \textbf{(2.2.19)}$$

with the modified formula:

$$\frac{z}{z_0}=\frac{4}{\pi}\cdot\sqrt{\frac{\pi}{2}}\frac{e^{-1\sqrt{\frac{1}{2}}}}{\sqrt{1}}\left\{\sin\left(\sqrt{\frac{1}{2}}+\frac{\pi}{8}\right)-\frac{1}{8}\sin\left(\sqrt{\frac{1}{2}}+\frac{3\pi}{8}\right)\right\}=0.608 \qquad \textbf{(2.2.20)}$$

because $a\cdot\alpha=1$ (see notation according to HERTZ 1884). It doesn't result in $\{0.646\}$ (see Table 2.2.1) because the function is valid for greater values of the radius. If I take for the radius $\rho=2\cdot\alpha$ then the Eq. 2.2.10 results with the original formula:

$$\frac{z}{z_0}=\frac{4}{\pi}\cdot\sqrt{\frac{\pi}{2}}\frac{e^{-2\sqrt{\frac{1}{2}}}}{\sqrt{2}}\left\{\sin\left(2\sqrt{\frac{1}{2}}+\frac{\pi}{8}\right)-\frac{1}{8\cdot2\alpha}\sin\left(2\sqrt{\frac{1}{2}}+\frac{3\pi}{8}\right)\right\}=0.267 \qquad \textbf{(2.2.21)}$$

and with the modified formlua:

$$\frac{z}{z_0} = \frac{4}{\pi} \cdot \sqrt{\frac{\pi}{2}} \frac{e^{-2\sqrt{\frac{1}{2}}}}{\sqrt{2}} \left\{ \sin\left(2\sqrt{\frac{1}{2}} + \frac{\pi}{8}\right) - \frac{1}{8 \cdot 2} \sin\left(2\sqrt{\frac{1}{2}} + \frac{3\pi}{8}\right) \right\} = 0.258 \qquad \textbf{(2.2.22)}$$

This result of the modified formula (Eq. 2.2.22) is equivalent to the value given by Hertz (see Table 2.2.1) For a greater radius with $\rho = 3 \cdot \alpha$ I achieve with the original formula:

$$\frac{z}{z_0} = \frac{4}{\pi} \cdot \sqrt{\frac{\pi}{2}} \frac{e^{-3\sqrt{\frac{1}{2}}}}{\sqrt{3}} \left\{ \sin\left(3\sqrt{\frac{1}{2}} + \frac{\pi}{8}\right) - \frac{1}{8 \cdot 3\alpha} \sin\left(3\sqrt{\frac{1}{2}} + \frac{3\pi}{8}\right) \right\} = 0.065 \qquad \textbf{(2.2.23)}$$

and by use of the modified formula:

$$\frac{z}{z_0} = \frac{4}{\pi} \cdot \sqrt{\frac{\pi}{2}} \frac{e^{-3\sqrt{\frac{1}{2}}}}{\sqrt{3}} \left\{ \sin\left(3\sqrt{\frac{1}{2}} + \frac{\pi}{8}\right) - \frac{1}{8 \cdot 3} \sin\left(3\sqrt{\frac{1}{2}} + \frac{3\pi}{8}\right) \right\} = 0.066 \qquad \textbf{(2.2.24)}$$

The results of Eq. 2.2.24 and from Hertz are equivalent (see Table 2.2.1). Therefore I conclude that the modified formula is correct.

2.2.3 Summary of the behavior of the functions

If I summarize the results (see Table 2.2.2) then I become an idea of the behavior of all functions.

	ratio z/z_0 calculated			
radius ρ	from Hertz	with logarithm function	with sine function	with **modified** sine function
α	0.646	0.646	0.657	0.608
$2 \cdot \alpha$	0.258	0.505	0.263	0.258
$3 \cdot \alpha$	0.66	0.072	0.065	0.66

Table 2.2.2) The results of the investigations are summarized for different values of radius.

Obviously the values are not correct if the radius is greater then $\rho = \alpha$ for the logarithm function and if the radius is smaller then $\rho = 2 \cdot \alpha$ for the sine-function. Conclusively the formala is divided into a close range - wide range, which can be described with the parameter α. Hence, a mathematical definition is received for the neighbourhood, the radius of action of the point load. The logarithm-function describes the vicinity and the sine-function works for the wide range. Between $\rho = \alpha$ and $\rho = 2 \cdot \alpha$ has to be the transition from the logarithm-function into the sine-function. In the following chapter I will modify all 3 functions. In order to retrieve one analytical solution for computation of the flexural rigidity, all the three functions will be unificate. Additionally some small errors could be found. I came to the conclusion that I have to use $(8\alpha\rho)^{-1}$ instead of $(8\rho)^{-1}$. In the following chapter all three formulas are investigated in order to apply them for the geological situation.

2.3 NEW ANALYTICAL SOLUTION

2.3.1 Introduction

VENING-MEINESZ (1939) used a modified form of HERTZ's flexure curve to compute the form of the compensation and computed a set of tables that summarized the total gravity effect of the compensation at a station for different assumed values of the parameter ß. This parameter has been evolved from the parameter α. It is a measure of the flexural rigidity of the plate and determines both the amplitude and wavelength of the compensation. In WATTS (2001), a modified form of the logarithm function is shown (see previous chapter, Eq. 2.2.9). But WATTS used only one solution to describe the deflection. For the next step all three functions will be merged in order to retrieve one analytical solution for the computation of the flexural rigidity. I found a concept for the dependence of the functions on the parameters ρ and α in Chapter 2.2, which I can use for a mathematical description in order to combine the three functions.

2.3.2 Modification and substitution

Hertz solved the equation for an ice plate and water as under laying substratum. He defined:

$$a^4 = \frac{12(1-\mu^2)}{Eh^3}s$$

with:
$$a^4 = \frac{1}{\alpha^4} \Rightarrow \alpha^4 = \frac{Eh^3}{12(1-\mu^2)} \cdot \frac{1}{s} \qquad \textbf{(2.3.1)}$$

The parameter h corresponds to $h = T_e$, and the Poisson's ratio corresponds to $\mu = \nu$. HERTZ (1884) did not take the gravity g into account. He considered only the specific density s of the underlying fluid. Furthermore he did not use a density contrast. Instead of a force $F = m \cdot g$ per unit area or a load, he considered a weight P.
However, if I want to apply this formula to the situation of the lithosphere, the Hertz solution has to be modified. Therefore I will consider the gravity within the weight P as well as in the unit from the Young's modulus E, because Hertz used as a unit $\left[\frac{kg}{m^2}\right]$. Hence, I attain a force F per unit area A with $\frac{F}{A} = \frac{mg}{1 \cdot m^2}$ which corresponds to a point load with $P = \rho \cdot g \cdot h$ (see Eq. 2.1.14) and receive therefore for the Young's modulus a unit $\left[\frac{N}{m^2}\right] \equiv [Pa]$. For the same reason, I will modify s with $s = (\rho_m - \rho_c)g$, (compare with Eq. 2.1.13) then it results: $\alpha = \beta$. Therefore it follows for the flexure parameter β:

$$\beta = \sqrt[4]{\frac{D}{(\rho_m - \rho_c)g}} \qquad \textbf{(2.3.2)}$$

with Eq.1.1.3 results: $$\beta^4 = \frac{ET_e^3}{12(1-\nu^2)} \cdot \frac{1}{(\rho_m - \rho_c)g} \qquad \textbf{(2.3.3)}$$

The equation, I want to solve, can be defined with the modern notation w for the deflection instead of z by: $$\Delta \cdot \Delta w + \frac{1}{\beta^4} w = 0 \qquad \textbf{(2.3.4)}$$

$\Delta w + w = 0$ I can solve according to HERTZ (1884) with $K(R) = \int_0^\infty e^{iR\cos iu} du$ for the radius $R^2 = x^2 + y^2$. Thereby is $K(\frac{R}{\sqrt[4]{-\beta}})$ one solution for Eq. 2.3.4, and it follows:

$$w = \frac{P}{4\pi\beta^2(\rho_m - \rho_c)g} \cdot \int_1^\infty \frac{e^{\frac{-R\sqrt{1/2}\xi}{\beta}} \sin\frac{R\sqrt{1/2}}{\beta}\xi}{\sqrt{\xi^2 - 1}} d\xi \qquad \textbf{(2.3.5)}$$

Instead of $R^2 = x^2 + y^2$ I use the substitution: $r_{x,y} = \frac{R}{\beta} = \frac{\sqrt{x^2 + y^2}}{\beta}$ as radial distance from the acting load. This results:

$$w = \frac{P}{4\pi\beta^2(\rho_m - \rho_c)g} \cdot \int_1^\infty \frac{e^{-r_{x,y}\sqrt{1/2}\xi} \sin r_{x,y}\sqrt{1/2}\xi}{\sqrt{\xi^2 - 1}} d\xi \qquad \textbf{(2.3.6)}$$

As a result I have a modified form of the Eq. 2.3.5. The first solution for the point of origin of the coordinate system is derived with the same procedure as in Chapter 2.2. According to the modification and the use of the Eq. 2.2.11 for the deflection w_0 results:

$$w_0 = \frac{P}{8(\rho_m - \rho_c)g \cdot \beta^2} \qquad \textbf{(2.3.7)}$$

This formula describes the maximum depth, because in the point where the load is acting, the deflection has a maximum value. For investigation of the neighborhood of point of origin, I can use the formula derived by Hertz (Eq. 2.2.9) for calculation of small values of the radius $r_{x,y}$. With $a = \frac{1}{\beta}$ (see Eq. 2.3.2) and the substitutions above follows $a\rho = \frac{\rho}{\beta}$ therefore is $a\rho = r_{x,y}$ and $r_{x,y} = \frac{\sqrt{x^2 + y^2}}{\beta}$ is the radial distance $[km]$ from the load, or radius respectively. With the substitution and modification results:

$$w(x,y)=\frac{P}{2\pi\beta^2(\rho_m-\rho_c)g}\cdot\left\{\begin{array}{l}\dfrac{(r_{x,y})^2}{2^2}\cdot\ln(r_{x,y})-\dfrac{(r_{x,y})^6}{2^2\cdot4^2\cdot6^2}\cdot\left(\ln(r_{x,y})-\dfrac{5}{6}\right)+\ldots\\ +\dfrac{\pi}{4}\left(1-\dfrac{(r_{x,y})^4}{2^2\cdot4^2}+\dfrac{(r_{x,y})^8}{2^2\cdot4^2\cdot6^2\cdot8^2}-\ldots\right)\\ \ldots-1.1159\cdot\left(\dfrac{(r_{x,y})^2}{2^2}-\dfrac{(r_{x,y})^6}{2^2\cdot4^2\cdot6^2}+\ldots\right)\end{array}\right\} \quad \textbf{(2.3.8)}$$

This Eq. 2.3.8 is shown in WATTS (2001), but with a small error. Instead of 4^2 is written 4^4. In the following I will call this solution "logarithm function". For greater values of the radius $r_{x,y}$ (this means the wide range of the solution), I will use according to Hertz the semi-convergent series (after radical expansion and integration of the single elements). With the substitution above follows:

$$w(x,y)=\frac{P}{2\pi\beta^2(\rho_m-\rho_c)g}\sqrt{\frac{\pi}{2}}\frac{e^{-(r_{x,y})\sqrt{\frac{1}{2}}}}{\sqrt{(r_{x,y})}}\left\{\sin\left((r_{x,y})\sqrt{\frac{1}{2}}+\frac{\pi}{8}\right)-\frac{1}{8(r_{x,y})}\sin\left((r_{x,y})\sqrt{\frac{1}{2}}+\frac{3\pi}{8}\right)+\ldots\right\}$$

(2.3.9)

Note: In view of the investigation in Chapter 2.2 I used the term $\frac{1}{8(r_{x,y})}$ *and not* $\frac{1}{8(r_{x,y})\cdot\beta}$ *!*

In the following I will call this derived solution from Eq. 2.3.9 "sine function".

2.3.3 Investigation of the graph

The behavior of the function for various elastic thicknesses $T_e=5;10;20;30;40km$ will be investigated. The analytical function was calculated for a point load with a height $h=1km$, Poisson's ratio $\upsilon=0.25$, Young's modulus $E=10^{11}Pa$, gravity $g=9.81m/s^2$, density of mantle $\rho_m=3350kg/m^3$ and density of crust $\rho_c=2700kg/m^3$.

In the following the logarithm function (see Eq. 2.3.8) is investigated (see Fig. 2.3.1). With increasing of the elastic thickness value T_e decrease the deflection in the point $w_0(0,0)$, but increase the distance $r_{x,y}$ of the bulge. Obviously it is not acceptable to use only the logarithm function to describe the flexure of an elastic plate, as this function breaks down after a certain distance.

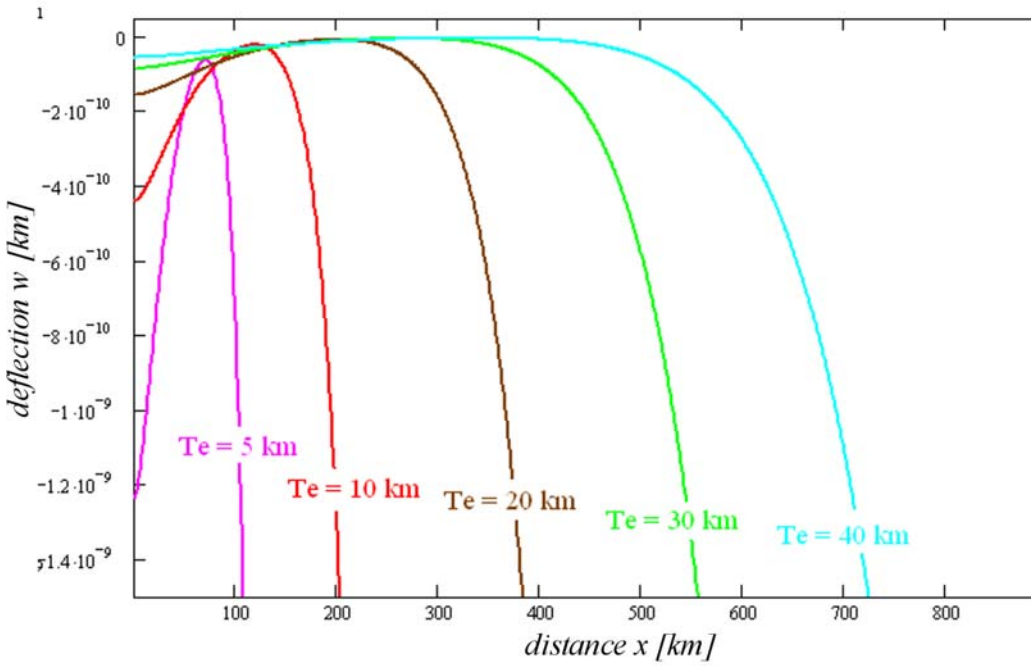

Figure 2.3.1) The Graph was calculated for the logarithm function for $T_e = 5;10;20;30;40km$. This function breaks down after a certain distance; therefore it is not acceptable to use only the logarithm function to describe the flexure of an elastic plate.

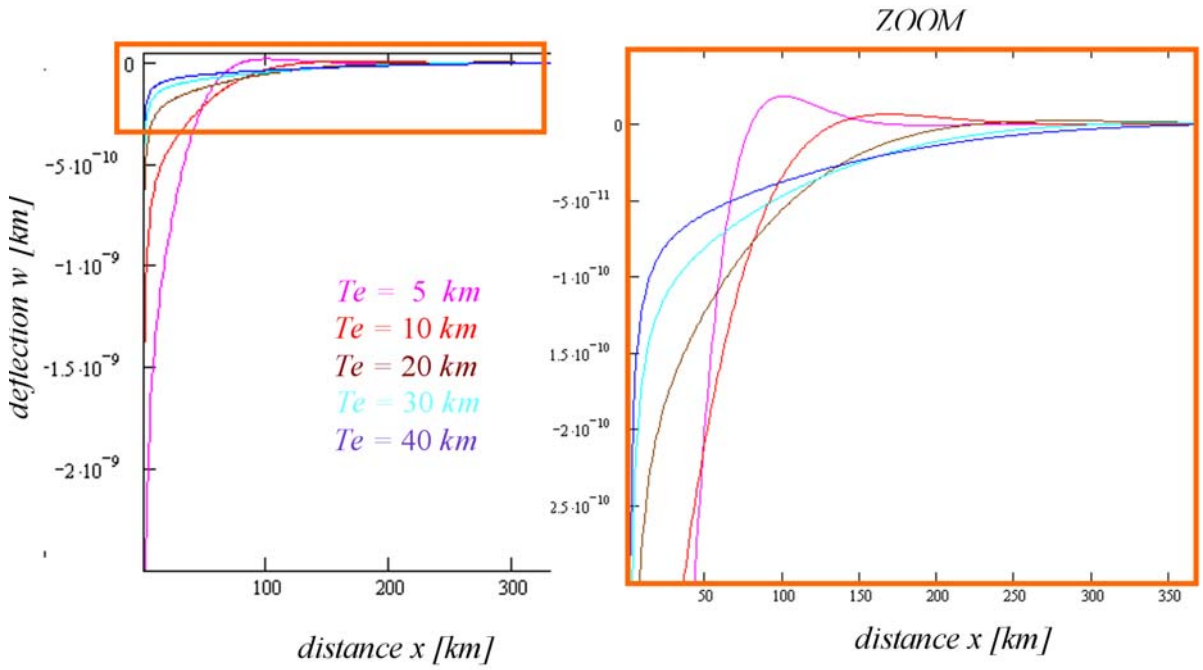

Figure 2.3.2) The graph was calculated for the sine function for $T_e = 5;10;20;30;40km$. The orange box characterizes the area of the zoom. The higher the bulge the lower is the elastic thickness value. The lower the elastic thickness value, the lower is the distance x at which the bulges occur.

In a next step the sinus function is considered (see Fig. 2.3.2). The same relationship is found for the elastic thickness value and the deflection w_0 and the distance of bulge, respectively. For illustration of the behavior of the function I will "zoom" in and study the bulges. The following relationship between the bulges and the elastic thickness value can be recognized: With increasing elastic thickness T_e, the amplitude of the bulge (positive w value) decreases.

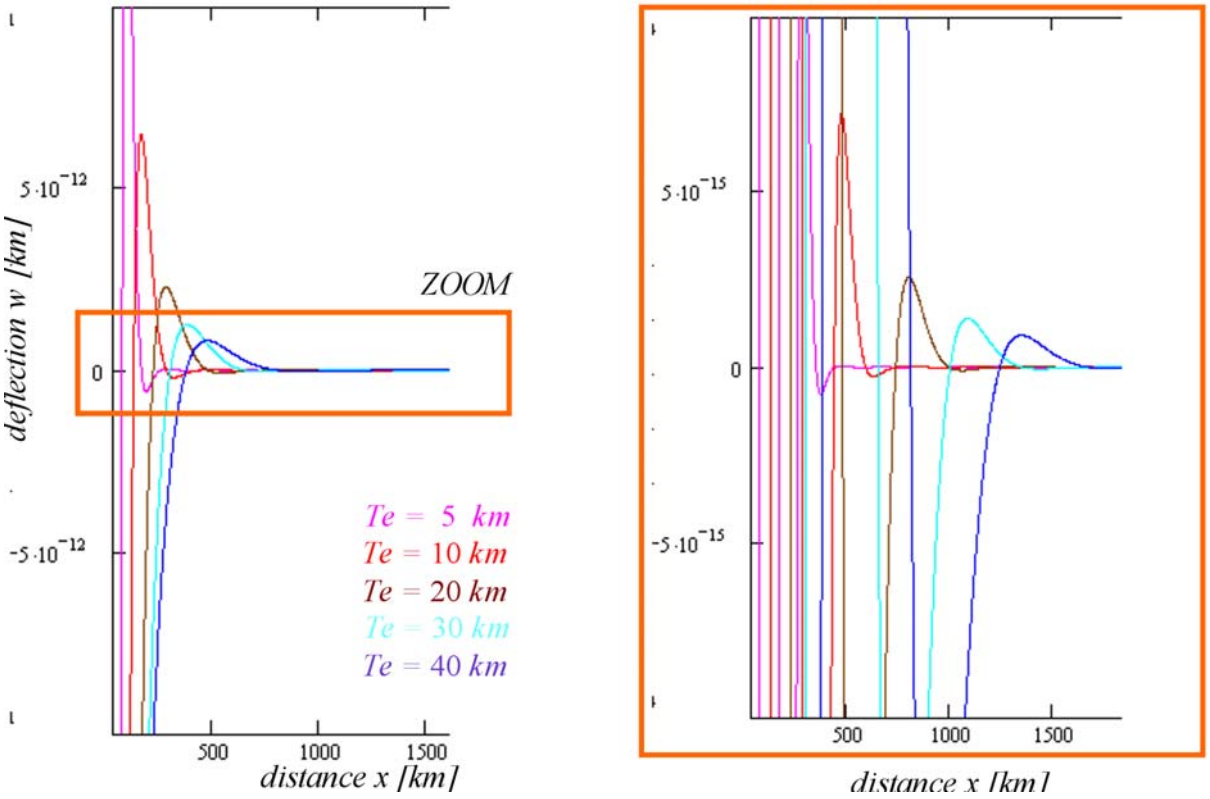

Figure 2.3.3) Graph for the sine function calculated for $T_e = 5;10;20;30;40km$, with further zoom. The orange box shows the area of zoom, whereby the second and the third bulges can be observed.

While further enlarging the graph, a second and third bulge can be observed (see Fig.2.3.3). A number of bulges occur that become infinite small (HERTZ 1884).
A simple analogue to illustrate the behavior of the sinus function is the "pattern" in the water when a stone is thrown into water. Where the stone hits the water several concentric bulges occurs, which become smaller with increasing distance from the center.

2.3.4 Unification of the analytical solution

I will combine all function according to the scheme, which was developed in Chapter 2.2. First the flexure parameter β is calculated with Eq. 2.3.3 for a point load with $h = 1km$, $T_e = 5km$, $\upsilon = 0.25$, $E = 10^{11} Pa$, $g = 9.81 m/s^2$, and the densities $\rho_m = 3350 kg/m^3$ and $\rho_c = 2700 kg/m^3$, therefore:

$$\beta^4 = \frac{10^{11}[N]\cdot(5000[m])^3}{12(1-(0.25)^2)[m^2]}\cdot\frac{[m^3 s^2]}{650[kg]\cdot 9.81[m]} \qquad \textbf{(2.3.10)}$$

and for the flexure parameter results:

$$\beta = \sqrt[4]{1.7425\cdot 10^{17}[m^4]} = 20431[m] \qquad \textbf{(2.3.11)}$$

The flexure parameter β and $2\cdot\beta$ is shown in Fig. 2.3.4. First the maximum deflection is calculated according to Eq. 2.3.7 and later compared with the result of the graph for the composite analytical solution. It results for the point load:

$$w_0 = \frac{2700[kg]\cdot 1000[m][m^3]}{8\cdot 650[kg]\cdot(20431[m])^2[m^3]} = 1.24\cdot 10^{-6} m \qquad \textbf{(2.3.12)}$$

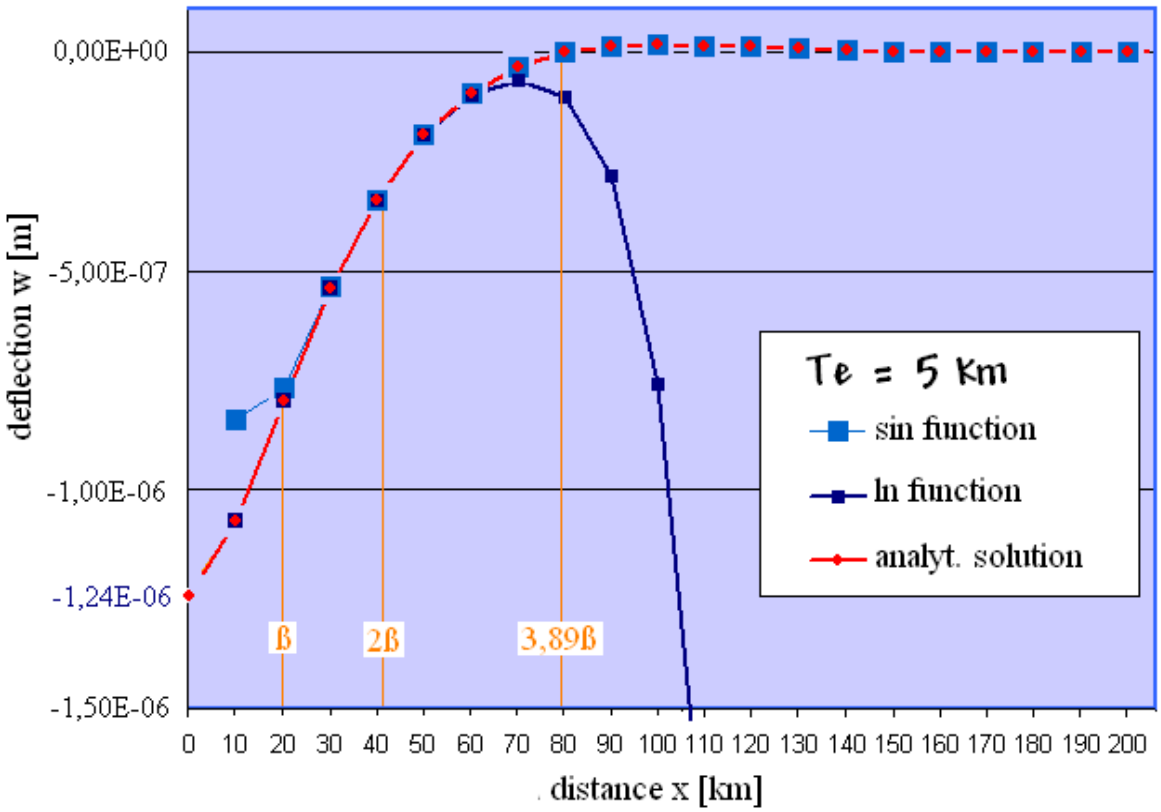

Figure 2.3.4) The graph for the composite analytical solution and the sine and logarithm function (colored in blue) was calculated for $T_e = 5km$. Additional, the flexure parameter is shown and the position of the bulge, which occurs at ca. $x = 3.89\cdot\beta$.

By comparison with the result (Fig.2.3.4) is obtained that in the point of origin, where the point load is acting, the value for w_0 is reached (blue colored). Furthermore it is obtained that the logarithm function is appropriate for the close range. On the other hand the values for the

deflection, produced by the sinus function, are too small in the close range. Therefore the analytical function has to switch from the logarithm function into the sinus function at a distance $r(x,y)=\beta$ and $r(x,y)=2\beta$. This was realized by the implementation of the composite analytical solution into a computer program for convolution by BRAITENBERG (PERS. COMM.).

The emergence of the first bulge at the distance x can be calculated with (HERTZ 1884):

$$x_{bu\lg e}=\frac{7}{8}\cdot\sqrt{2}\cdot\pi\cdot\beta=3.89\cdot\beta=79.48km \qquad \textbf{(2.3.13)}$$

According to HERTZ (1884) the deflection results at the bulge $w(x_{bu\lg e})=0km$, and the value for the deflection w becomes positive with increasing radial distance. I found that this is valid for the sinus function only (see Fig.2.3.4). This is another evidence for the idea that the logarithm function is not suitable for the greater values of distance or radius, respectively.
However, another item can be concluded with this investigation for the bulge. In order to accelerate further calculation, the analytical function should be cut at a certain distance. In view of the fact that the deflection value should reach zero before the function is cut, the function should be considered within the distance $x_{bu\lg e}=3{,}89\cdot\beta$. I will apply these suggestions for the radius of convolution (see Chapter 2.6).

2.4 TRANSFER FUNCTION

2.4.1 Introduction

The lithosphere does not respond locally to long-term geological loads, as the AIRY and PRATT models would predict. As described in Chapter 1, the compensation takes place regionally by a flexure over a wide region. Thereby the lithosphere behaves as a filter suppressing the short-wavelength deformation (large amplitude) associated with local models of isostasy and passes the long-wavelength deformation (small amplitude) corresponding to the flexural behavior of the lithospheric plate. The expression "filter" is used in its usual meaning to describe a system with input and output. The input is the load and the output is the flexure. The assumption is that the lithosphere behaves like a linear space-invariant filter (WATTS 2001). This means that if a topographic load with height $h(x)$ causes a deflection $w(x)$ and a topographic load with height $\hat{h}(x)$ produces a flexure $\hat{w}(x)$ then the sum $h(x)+\hat{h}(x)$ generate a flexure of $w(x)+\hat{w}(x)$. Another property of such a filter is, that if the input load is periodic, then the output flexure is also periodic. The general equation describing the elastic response of a plate to a periodic load is given for one dimension by:

$$D\frac{\partial^4 w}{\partial x^4}+(\rho_m-\rho_i)gw=(\rho_c-\rho_w)gh\cdot\cos(kx) \qquad \textbf{(2.4.1)}$$

with D as the flexural rigidity, w as the flexure, x as the horizontal distance, ρ_m as the density of the mantle, ρ_i as the density of the material that infills the flexural depression, ρ_c as the density of the crust, ρ_w as the density of the medium which displaces the load (e.g. water, air), h as the peak-to-through amplitude of the load and k as the wavenumber of the load in the x direction, respectively. The solution of Eq. 2.4.1 is periodic and has the form:

$$w=\frac{(\rho_c-\rho_w)\cdot h\cdot\cos(kx)}{(\rho_m-\rho_i)}\left[\frac{D\cdot k^4}{(\rho_m-\rho_i)\cdot g}+1\right]^{-1} \qquad \textbf{(2.4.2)}$$

For a weak plate, the rigidity approaches zero. For $D\to 0$ the Eq. 2.4.2 leads to :

$$w\to\frac{(\rho_c-\rho_w)\cdot h\cdot\cos(kx)}{(\rho_m-\rho_i)} \qquad \textbf{(2.4.3)}$$

if I additionally assume $\rho_i\equiv\rho_c$, then I achieve the Airy isostatic response to a periodic load:

$$w\to\frac{(\rho_c-\rho_w)\cdot h\cdot\cos(kx)}{(\rho_m-\rho_c)} \qquad \textbf{(2.4.4)}$$

For an endless rigid plate the flexure approaches zero. For $D \to \infty$ the Eq. 2.4.2 approaches zero $w \to 0$. This is called Bouguer response. If the plate has a finite strength, then it responses by a flexure. Chapter 1.2 introduces the isostatic response function. A wave-number parameter $\Phi_e(k)$ is defined, modifying the gravity effect of the topography such as to produce the gravity anomaly. It is given with (see Chapter 1.2):

$$\Phi_e(k) = \frac{output}{input} \qquad \textbf{(2.4.5)}$$

If this wave-number parameter $\Phi_e(k)$ is used to modify the Airy response such as to create the flexure, the input and the output (see Eq. 2.4.2) of the system is given with (WATTS 2001):

$$input = \frac{(\rho_c - \rho_w) \cdot h \cdot \cos(kx)}{(\rho_m - \rho_i)} \qquad \textbf{(2.4.6)}$$

$$output = \frac{(\rho_c - \rho_w) \cdot h \cdot \cos(kx)}{(\rho_m - \rho_i)} \left[\frac{D \cdot k^4}{(\rho_m - \rho_i) \cdot g} + 1 \right]^{-1} \qquad \textbf{(2.4.7)}$$

from the Eq. 2.4.5 follows: $$\Phi_e(k) = \left[\frac{D \cdot k^4}{(\rho_m - \rho_i) \cdot g} + 1 \right]^{-1} \qquad \textbf{(2.4.8)}$$

From Eq. 2.4.5 follows that $\Phi_e(k)$ determines the wavenumber for which the flexure is important. This parameter is called “flexural response function” (WALCOTT 1976).

2.4.2 Transfer function

However, Eq. 2.4.8 yields only the flexural response to a load at a particular wavenumber. Since a load can be split into its individual spectral components, Eq. 2.4.2 can be used to compute the response to any arbitrarily shaped load. The method of Fourier analysis (see Chapter 1.2) is a widely used technique to decompose a spatial data set into its spectral components. Replacing the term $h \cdot \cos(kx)$ in Eq. 2.4.2 by $H(k) = FT[h(x)]$, which represents the wave number domain of the topography $h(x)$ and replacing the flexure $w(x)$ with $W(k) = FT[w(x)]$, which is the description for the wave number domain; yields to (WATTS 2001):

$$W(k) = \frac{(\rho_c - \rho_w) \cdot H(k)}{(\rho_m - \rho_i)} \left[\frac{D \cdot k^4}{(\rho_m - \rho_i) \cdot g} + 1 \right]^{-1} \qquad \textbf{(2.4.9)}$$

with use of Eq. 2.4.8 :

$$W(k) = \frac{(\rho_c - \rho_w)}{(\rho_m - \rho_i)} \varphi_e(k) \cdot H(k) \qquad \textbf{(2.4.10)}$$

In order to describe the flexural response for a point load the impulse function $\delta_d(x)$ can be used. The impulse function is defined as (BRIGHAM 1974):

$$\delta_d(x) = 0 \;\; \forall x \neq 0 \quad \text{and} \quad \int_{-\infty}^{\infty} \delta_d(x)dx = 1 \qquad \textbf{(2.4.11)}$$

This is the mathematical description for the fact that the value of a point load is 1 and the extension of this point load is 0. This condition mathematically means that $h(x) = \delta_d(x)$ and therefore $H(k) = FT[h(x)] = 1$. According to Eq. 2.4.10 and with $H(k) = FT[h(x)] = 1$ result:

$$W(k) = \frac{(\rho_c - \rho_w)}{(\rho_m - \rho_i)} \varphi_e(k) \qquad \textbf{(2.4.12)}$$

Hence I receive the flexural response for a point load. This study reveals that the Fourier analysis is the equivalent in the space domain to a convolution of an impulse function with discrete samples of a load (see Fig. 2.4.1).

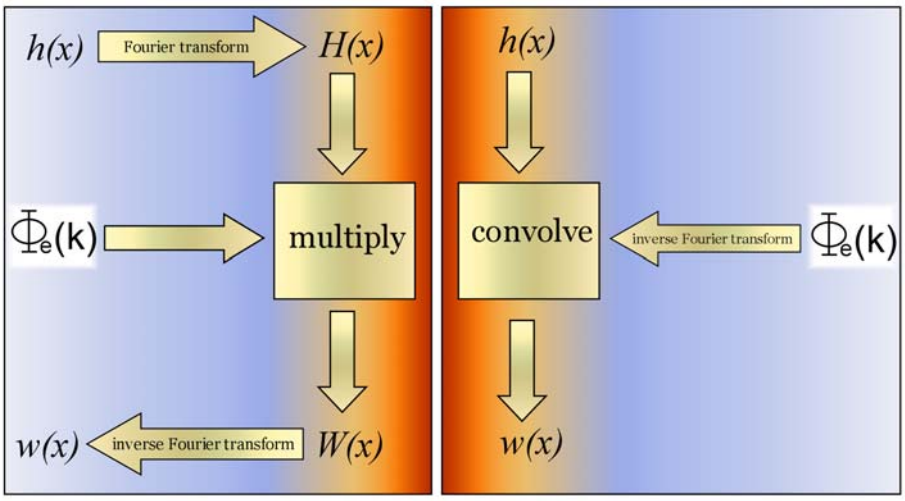

Figure 2.4.1) The scheme presents the principal steps of filtering of a topographic data set in the frequency domain (on the left side) and space domain (on the right side), modified from WATTS (2001), thereby the analytical solution has to be equivalent to the inverse Fourier transform of the flexural response function.

The spatial variation of the flexure is obtained by using the Fourier transform of the load, by multiplying it with the wavenumber parameter and a density term; afterwards the inverse transform of the result is calculated. In the space domain this is equivalent to the convolution of the load with the inverse Fourier transform of the wavenumber parameter and the density term. For $\Phi_\delta(k) = \frac{(\rho_c - \rho_w)}{(\rho_m - \rho_i)} \varphi_e(k)$ and Eq. 2.4.8 it follows:

$$\Phi_\delta(k) = \frac{(\rho_c - \rho_w)}{(\rho_m - \rho_i)}\left[\frac{D \cdot k^4}{(\rho_m - \rho_i)\cdot g} + 1\right]^{-1} \qquad \textbf{(2.4.13)}$$

With use of Eq. 2.4.9 : $$W(k) = \Phi_\delta(k) \cdot H(k) \qquad \textbf{(2.4.14)}$$

Therewith I obtain a transfer function to describe the flexure of a point load. This function I is used for verification of the analytical solution, as the analytical solution also computes a flexure to any arbitrarily shaped load. The inverse Fourier transform of the Eq. 2.4.13 has to give the same result as the flexure curve computed by the analytical solution (see Fig. 2.4.1). Vice versa the Fourier transform of the flexure curve calculated with the analytical solution has to be the same like the curve that results from Eq. 2.4.13.
Hence, the Fourier transform of the flexure curve has to be computed after convolution with a point load (= delta function). The resulting function is notated with Φ_{analyt} in the following.
In the analytical solution the density ρ_w of the medium displacing the load (e.g. water, air) is not considered. This is done in a next step with the convolution of a special input grid. The idea of a density of the material that infills the flexural depression ρ_i is better described by internal density variation within the crust. The internal loads are taken into account (PERS. COMM. GÖTZE) with the concept of pseudo topography (Chapter 1.4). Accordingly, if I want to compare the results with the analytical solution, I have to set the density of the material that infills the flexural depression ρ_i equal to the crustal density of ρ_c. Neglecting the density ρ_w and using $\rho_i = \rho_c$ the Eq. 2.4.13 leads to:

$$\Phi_\delta(k) = \frac{(\rho_c)}{(\rho_m - \rho_c)}\left[\frac{D \cdot k^4}{(\rho_m - \rho_c)\cdot g} + 1\right]^{-1} \qquad \textbf{(2.4.15)}$$

Finally I obtain a transfer function $\Phi_\delta(k)$, which I compare with Φ_{analyt}, the Fourier transform of the flexure curve computed with the analytical solution after convolution with a point load.

2.4.3 Verification of the analytical solution

In order to prove the analytical solution the response function Φ_{analyt} is compared with the transfer function $\Phi_\delta(k)$. Accordingly, I compute (Eq. 2.4.15) with the wave numbers $1\cdot10^{-5} \le k \le 1\cdot10^{-4}$ and with the densities $\rho_c = 2700 kg/m^3$ and $\rho_m = 3350 kg/m^3$ the graph of the flexural response $\Phi_\delta(k)$. The transfer function Φ_{analyt} is the Fourier transform of the flexure curve after convolution with a point load. It arises that the transfer function Φ_{analyt} is equivalent to $\Phi_\delta(k)$ except for a specific factor. This factor is independent of T_e, and unfortunately not explainable.

However, intense investigations lead to following clarification. By varying all parameters a dependency is found for the distance dx and dy of the nodes of the input grid for the point load. The factor I can summarize with:

$$fact = \frac{1}{dx \cdot dy} \qquad \textbf{(2.4.16)}$$

Referring to the assumptions this factor is explainable: In the original formula a force per unit area was considered, which was transformed to a point load. This assumption is not valid for an input grid. This leads to the factor corresponding to the formerly neglected unit area. The comparison of the two transfer functions Φ_{analyt} and $\Phi_{\delta}(k)$ is shown in Fig. 2.4.2.

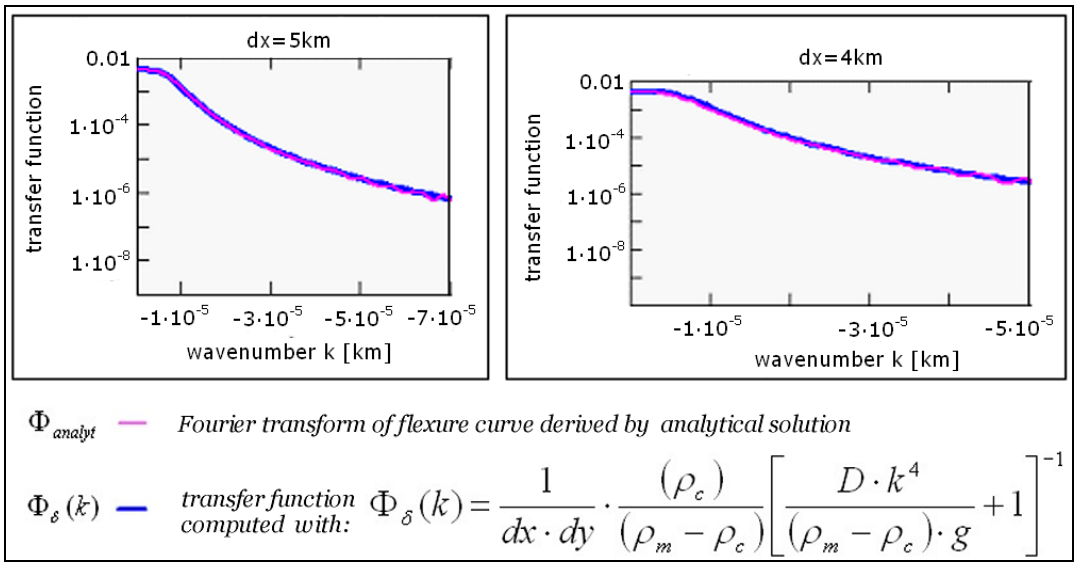

Figure 2.4.2) Comparison of transfer function computed for $T_e = 1km$. The transfer function Φ_{analyt} (pink colored) is equivalent to $\Phi_{\delta}(k)$ (blue colored) in Eq. 2.4.15, except to $fact = dx \cdot dy$ whereby dx and dy node distance of input grid. On the left side the node distance is $dx = dy = 5km$ and on the right side $dx = dy = 4km$.

2.4.4 Conclusion

Accordingly there is evidence for the correct calculation of the flexure by the analytical solution. In the next chapter I will show that the flexure curves in the space domain calculated by the analytical solution are equal to the flexure curves from the inverse Fourier transform of the response function $\Phi_{\delta}(k)$. Then I will compare the input flexure curves of the convolution software according to BRAITENBERG (ET AL. 2002) with the flexure curves derived by the analytical solution.

2.5 COMPARISON WITH FFT METHOD

In Chapter 2.4 I conclude that the analytical solution is equivalent to the inverse Fourier transform of the flexural response function. In the following the inverse Fourier transform of the flexural response function is called "flexure curve from FFT".
The dependence of the analytical solution from the distance of the grid nodes is evaluated by comparison of the flexure curve from FFT with the analytical solution.
Furthermore, if a new solution is introduced, then this solution has to fit into well-accepted theories (PERS. COMM. WIENECKE J.); therefore boundary cases of the new analytical solution are considered. An example is shown for a real topography in a general and a phenomenological form. Thereby the location and the geological features are not important. The focus lies on the behavior of the analytical solution in order to understand the general principles.

2.5.1 Comparison with flexure curves

The comparison is done with the flexure curves from FFT and the analytical solution calculated for a point load with height $h = 1km$ and the following parameters: elastic thickness $T_e = 5km$, Poisson's ratio $\nu = 0.25$, Young's modulus $E = 10^{11} Pa$, gravity $g = 9.81 m/s^2$, densities of mantle $\rho_m = 3350 kg/m^3$ and crust $\rho_c = 2700 kg/m^3$.

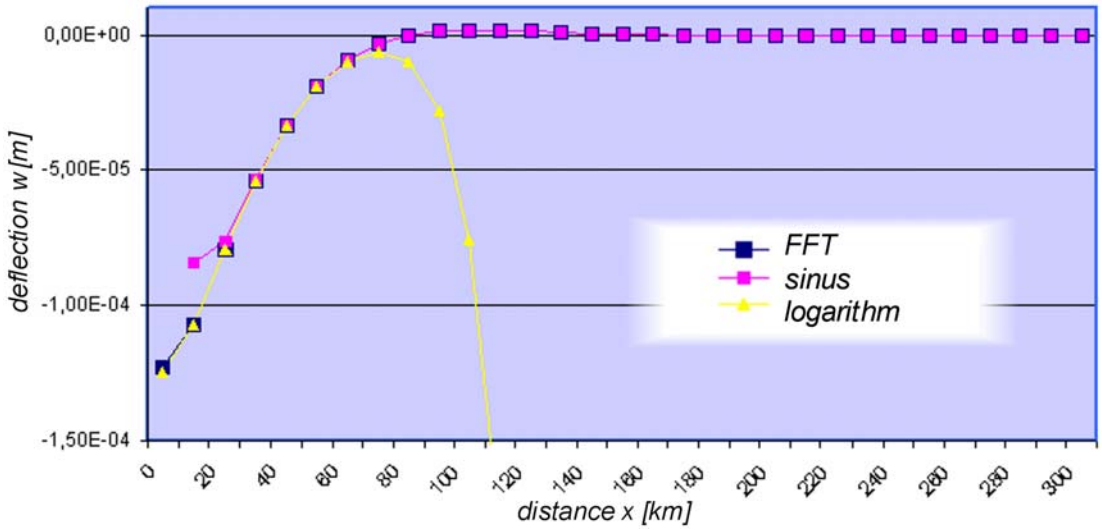

Figure 2.5.1) The flexure curves for $T_e = 5km$ from the FFT (in blue color) and the modified analytical solution is presented: the sinus function (pink colored) and the logarithm function (yellow colored). The analytical solution fits to the FFT flexure curve with exception to the factor $fact = 10^5$.

An input grid of delta topography creates the point load. The input grid consists of several numbers of nodes, notated with n in x direction and m in y direction, and the distance between the nodes dx, dy. The flexure curves from FFT and the analytical solution are

plotted at the same scale. Hence, due to a graphical analysis the value of $fact$ is estimated. The result for $T_e = 5km$ is shown in Fig. 2.5.1. Further graphical analysis for $T_e = 10;20;30;40km$ is presented in the appendix (Chapter 5.2.1). Various T_e values have been used for the calculation with different values of dx, dy. Table 2.5.1 displays the resulting factors according this inspection. For $T_e = 20;30km$ are the same values of $dx, dy[m]$ used. Recognizing, that the factor is equal, I assume a relationship between the distance of the grid nodes and the factor, describing the disagreement of the flexure curves. As described in Chapter 2.4 the same relationship $fact = dx \cdot dy$ is obtained.

$dx, dy[m]$	$T_e[km]$	$fact = 10^5$
10000	5	1
15000	10	2,25
20000	20	4
20000	30	4
30000	40	9

Table 2.5.1) The factor between the flexure curves is calculated with analytical solution and with spectral methods (FFT) in dependence of the node distance of input grid of delta topography

2.5.2 Investigation of dependence from grid parameters

I have to assume the factor either in the flexure curves from the FFT or in the analytical solution. The dependence of the numbers of grid nodes n, m is investigated in addition.

Delta topography

The investigation of a dependence of the flexure calculation from the grid parameter of delta topography, I examine the values of maximum deflection for different numbers of nodes n, m but same for the distances of the grid nodes dx, dy (see Table 2.5.2).

calculated with analytical solution			calculated with Fourier transform		
grid nodes n, m	grid distance dx, dy	max. value w_0	grid nodes n, m	grid distance dx, dy	max. value w_0
220	5000	$-1.24 \cdot 10^{-12}$	260	5000	$-3.10 \cdot 10^{-5}$
550	5000	$-1.24 \cdot 10^{-12}$	650	5000	$-3.10 \cdot 10^{-5}$

Table 2.5.2) The maximum value of deflection of flexure curves is examine for different nodes numbers n and m of input grid for delta topography.

The values of maximum deflection of the flexure curves from the FFT and from the analytical solution are independent on the number of grid nodes n, m. In the following I calculate the maximum deflection w_0 for different dx, dy but for same amount of n, m (see Table 2.5.3).

calculated with analytical solution			calculated with Fourier transform		
grid nodes n, m	grid distance dx, dy	maximal value w_0	grid nodes n, m	grid distance dx, dy	maximal value w_0
550	2000	$-1.24 \cdot 10^{-12}$	650	2000	$-4.97 \cdot 10^{-6}$
550	5000	$-1.24 \cdot 10^{-12}$	650	5000	$-3.10 \cdot 10^{-5}$

Table 2.5.3) The maximum value of deflection of the flexure curves is calculated for different distance of input grid for delta topography.

The values of the analytical flexure curve are independent on the distance dx, dy. The values of the maximal deflection vary with different distances of the grid nodes for the flexure curves calculated with the FFT method. In view of that, the flexure curves from the FFT are multiplied with the factor $fact = \frac{1}{dxdy}$, producing the same results (see Table 2.5.4).

grid distance	analytical solution	Fourier transform	Fourier transform multiplied with $fact = \frac{1}{dxdy}$
dx, dy	w_0	w_0	w_0
5000	$-1.24 \cdot 10^{-12}$	$-3.10 \cdot 10^{-5}$	$-1.24 \cdot 10^{-12}$
4000	$-1.24 \cdot 10^{-12}$	$-1.99 \cdot 10^{-5}$	$-1.24 \cdot 10^{-12}$
2000	$-1.24 \cdot 10^{-12}$	$-4.97 \cdot 10^{-6}$	$-1.24 \cdot 10^{-12}$

Table 2.5.4) The maximum value of deflection of the flexure curves is calculated by multiplication with the grid node distance.

However, considering the input grid for delta topography, it is seen that the topographic load is changing in dependence of the distance dx, dy (see Figure 2.5.2), because of the computational interpolation of a point load of the height $h = 0$ to $h = 1$. With increasing of the distance dx, dy the area of the delta topography grows, which leads to an increase of the deflection. Conclusively, the maximum deflection calculated for delta topography must increase along with an increase of dx, dy. Therewith it is established that the flexure curves from the FFT are dependent on dx, dy. Consequently, the maximum deflection calculated with the analytical solution necessarily changes with dx, dy, investigated in the following for

a synthetic topography, since in this case the interpolation problems mentioned above are diminished.

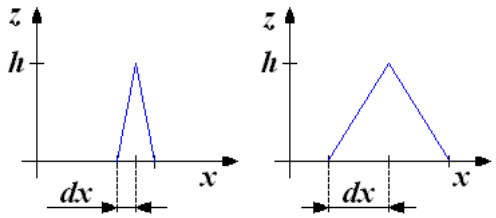

Figure 2.5.2) The Delta topography is shown for a small distance of grid nodes dx on the left and for a larger dx on the right. Despite of a constant height of load, the load effect enlarges with increasing of the distance dx.

Synthetic Topography

I compute the maximum deflection of the flexure curves from the FFT and from the analytical solution with the same synthetic topography (Table 2.5.5). Both flexure curves are independent on n, m from the input grid. The flexure curves from the FFT are independent on dx, dy for a synthetic topography.

calculated with analytical solution				calc. with Fourier transform		
grid node number n, m	grid distance dx, dy	maximal value w_0	multiplied with $fact = dy \cdot dx$ max. value w_0	grid node number n, m	grid distance dx, dy	maximal value w_0
220	5000	$-4.98 \cdot 10^{-7}$	$-1.25 \cdot 10^{1}$	260	5000	$-1.24 \cdot 10^{1}$
550	2000	$-3.11 \cdot 10^{-6}$	$-1.25 \cdot 10^{1}$	650	2000	$-1.24 \cdot 10^{1}$

Table 2.5.5) The maximum value of deflection of the flexure curves is calculated for a synthetic topography.

The multiplication of the analytical solution with the distance of the input grid nodes leads to the same result for the maximum deflection. Accordingly I come to the following conclusions for the analytical solution:

1. the analytical solution is dependent on the input grid of topography
2. the flexure curves must be calibrated, before start of the convolution
3. the calibration is done by multiplication with the distance of nodes dx, dy for all input grids (e.g. point load, synthetic topography and pseudo topography)
4. the output of the flexure curves are different from the output of the CMI surface (additional to the shift due to the reference depth)

This calibration by multiplication of the analytical solution is implemented within the computer software “coto” (described in Chapter 2.6). Once again the solution from “coto” is to be compared with the flexure curves from the FFT: The graphical comparison of that is

presented in the appendix (Chapter 5.2.2). A very good agreement is obtained with both flexure curves. In view of that the verified analytical solution is applicable on a real topography.

2.5.3 Boundary cases for elastic thickness

A new solution introduced, has to fit into well-accepted theories. Since the classical Airy model for local compensation corresponds to a flexural model where the plate has no strength (see Chapter 1.1.4. , Fig. 1.2.4), I inspect the analytical solution for a small value of elastic thickness $T_e = 1km$. Furthermore I conclude (see Chapter 1.1.4) that with an increase of the elastic thickness the undulation of the CMI lowers. Therefore with higher values of the elastic thickness parameter the surface must converge to a flattened plane with a constant value of the CMI depth. I set these ideas into application with the analytical solution for a real topography. If the analytical solution is comparable to these boundary cases, then an evidence for the correct calculation of the analytical solution is found. Firstly the CMI depth variation is calculated with the analytical solution for a small elastic thickness value $T_e = 1km$, with the load model of the Pacific Ocean as input grid (for further investigation see Chapter 3.1). The comparison of the two CMI surfaces calculated with the analytical solution and with the Airy solution is displayed in Fig. 2.5.3.

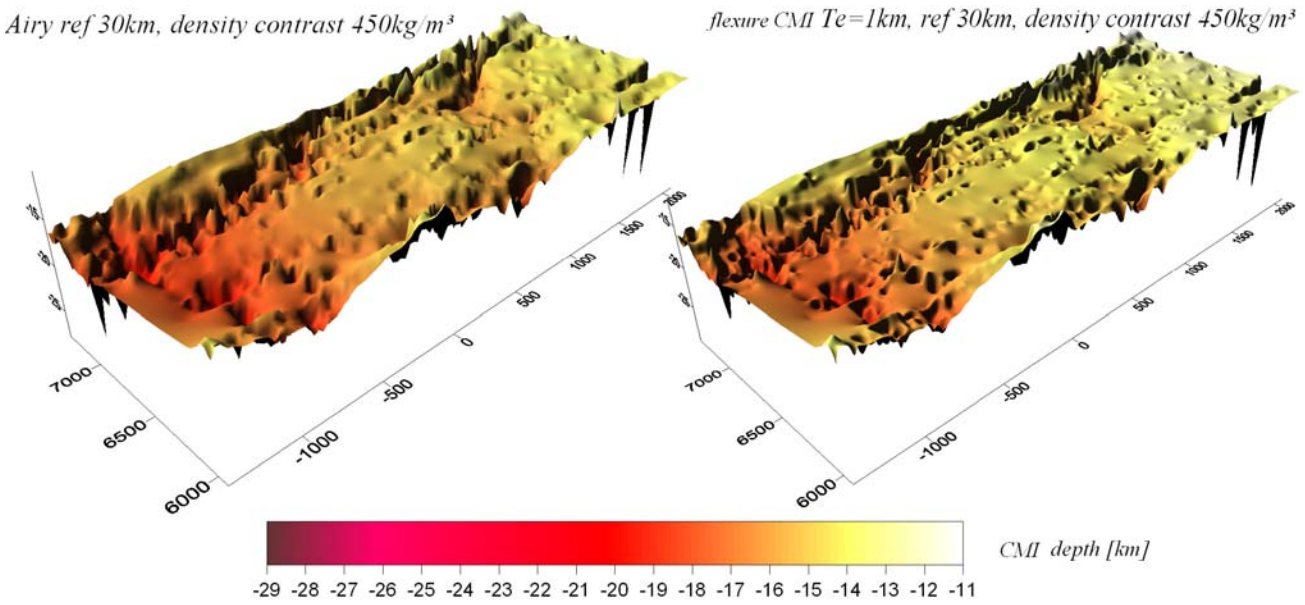

Figure 2.5.3) The CMI surfaces are computed with the analytical solution for $T_e = 1km$ and with the Airy solution. The input grid is the load model of the Pacific Ocean in both cases.

The Airy solution is computed with the software "INTERP" (LAHMEYER 1989) with FFT techniques using the same input parameters. Both CMI surfaces are similar to each other showing the same flexural behavior. Subsequently the difference-grid of both CMI's is calculated and overlain on the bathymetry. The *RMS* values range below $0.5km$, the median difference value is $0.15km$ with a standard deviation of 0.48 (Figure 2.5.4).

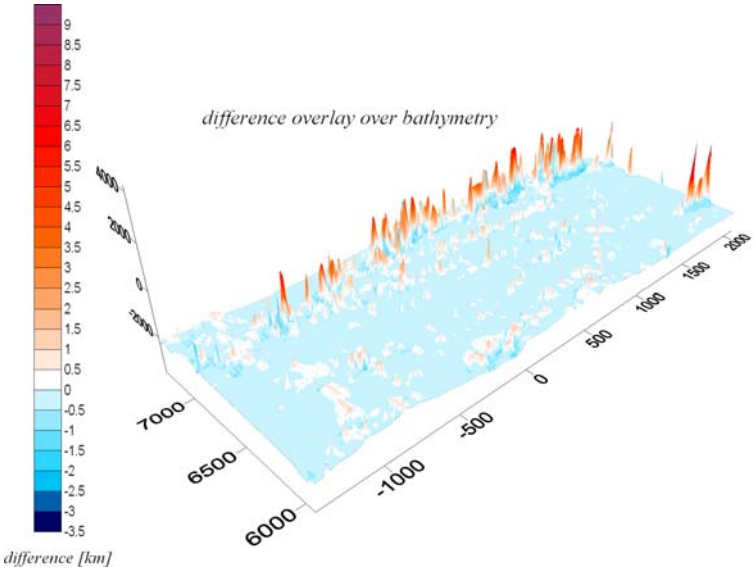

Figure 2.5.4) The difference values of CMI depth are overlain over the bathymetry.

Since the greater CMI differences occur in the area of the seamounts it is verified that the analytical solution is converging to the Airy solution. Subsequently, the analytical solution for high elastic thickness values is investigated. As an example the area of the Southern Andes is chosen (see Chapter 3.3). Figure 2.5.5 illustrates the CMI undulation, computed with the analytical solution with different T_e values and with a reference depth of $30km$. As a result CMI surface flattens with an increase of the elastic thickness value; the undulation decreases and the CMI surface converges to a plane of one constant depth.

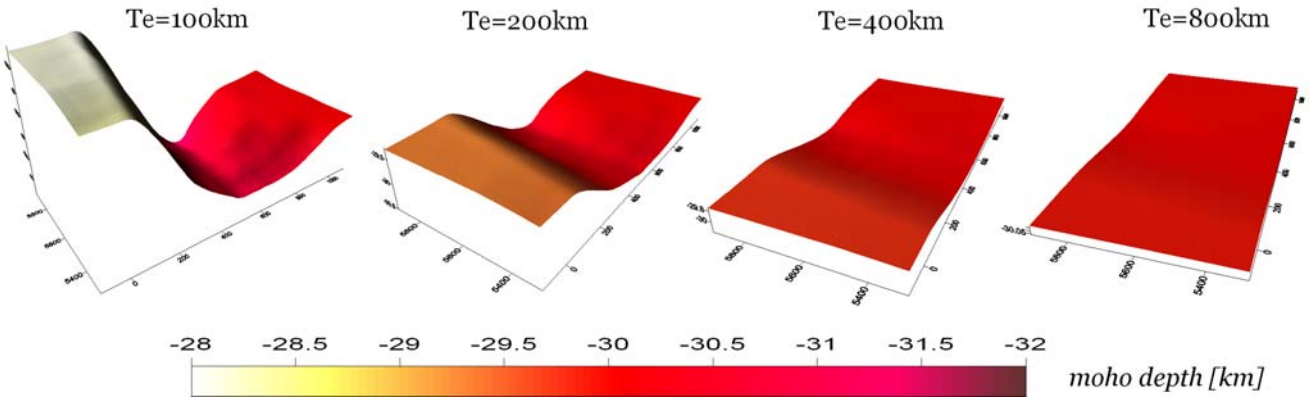

Figure 2.5.5) The CMI surfaces are calculated with the analytical solution with increasing values of the elastic thickness. Along with increasing of the T_e values the CMI depth undulations decrease.

The maximum and minimum values of the CMI depths are investigated (see Table 2.5.6). Conclusively the value of the deflection converges to the value of the reference depth (e.g. of $30km$ in the case of the Southern Andes).

Input parameter elastic thickness T_e	Output CMI		difference
	maximum depth w	minimum depth w	
100	-31,3572	-28,0501	-3,30706
400	-30,185	-29,7332	-0,4518
800	-30,0662	-29,9045	-0,16163
3200	-30,0083	-29,988	-0,02034
9000	-30,0018	-29,9975	-0,00432

Table 2.5.6) The maximum/minimum value of the depths of the CMI's are compared for various values of the elastic thickness.

2.5.4 Comparison with Vening-Meinesz solution

Vening-Meinesz used a modified form of the second Hertz's equation. Since the analytical solution was developed out of all three Hertz's solution, it should approach the Vening-Meinesz solution. The analytical solution includes the solution for the maximum deflection w_0 at the point of origin leading to a higher resolution for even small values of the input topography. In opposition to this the Vening-Meinesz solution (Chapter 1.1.3) solved in the frequency domain (BANKS ET AL. 1977) , results in instabilities with small values of the input topography.

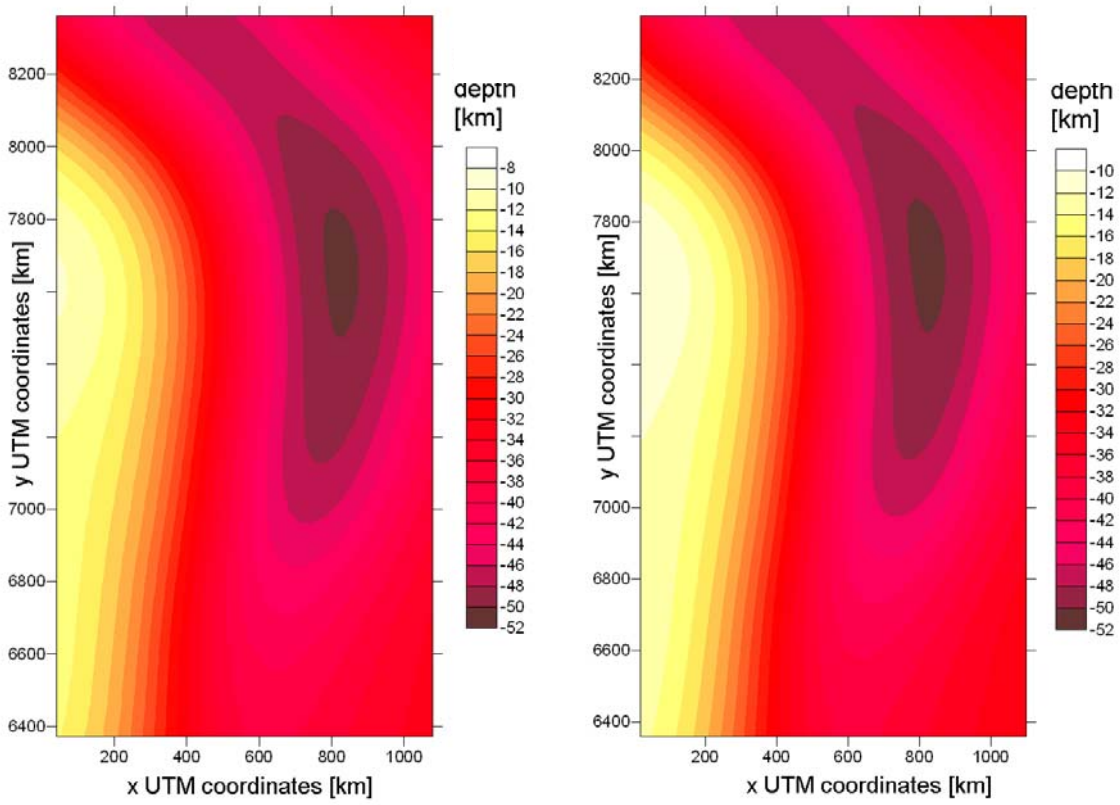

Figure 2.5.6) The CMI estimated from FFT (on the left side) is compared with the CMI computed with the analytical solution (on the right side) for the same input parameter.

Furthergoing investigations are done for the topography of the Central Andes (see Chapter 3.2). A CMI is computed with the FFT with the software "INTERP" (LAHMEYER 1989) with a rigidity of $D = 2.4 \cdot 10^{24}\, Nm$ and with the same isostatic model parameters: $\rho_m = 3380 kg/m^3$, $\rho_c = 2900 kg/m^3$, $\rho_w = 1030 kg/m^3$ and a reference depth of $30 km$ (shown in Figure 2.5.5). A good agreement with both CMI surfaces is found: The difference of the two output grids ranges between $-0.65 km \le \Delta w \le 0.65 km$ (see Fig. 2.5.6). In view of the fact that the values of the CMI depths range from $-52 km \le w \le 8 km$ a very good conformity between the analytical solution and the Vening-Meinesz solution is obtained.

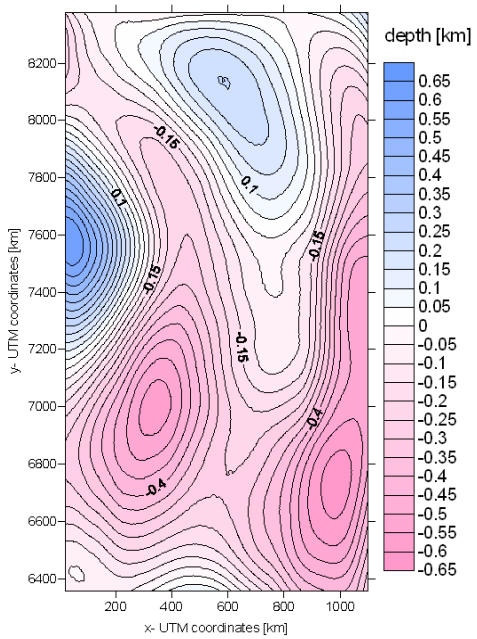

Figure 2.5.7) The difference-grid between the CMI surfaces is computed with the Vening-Meinesz solution and the analytical solution. The values of differences range between -0,65 km (pink colored) and + 0,65 km (blue colored) .

2.5.5 Conclusion

The flexure curves calculated with the analytical solution are equivalent to the inverse Fourier transform of the flexural response function. It is necessary to multiply the analytical solution with the factor $fact = dx \cdot dy$ of the distance of the input grid nodes. The analytical solution is verified by comparison with the flexure curves from FFT for a point load and a synthetic topography. I also demonstrate for a real topography that the analytical solution approaches to the Vening-Meinesz solution. Therefore evidence for the correct calculation of the analytical solution is found.

Furthermore I show that this new solution is fitting into the well-accepted theories. For small values of T_e the solution converges to the Airy solution; for high values of T_e the undulation of the CMI surface decreases.

2.6 SOFTWARE CONCEPT

2.6.1 Introduction

In the following the results of the analytical solution are investigated. The application for various study areas is represented in a general and phenomenological form. The focus is not on the location and the geological features, but spots on the behavior of the analytical solution in order to understand the general principia. The study areas are considered in detailed in Chapter 3. The float chart (Fig. 2.6.1) illustrates the single steps during the computation of the elastic thickness/flexural rigidity variation. The software developed by BRAITENBERG (PERS. COMM.) convolves the flexure curves with the input load grid in order to estimate the crust mantle interface: This so called "flexure CMI" corresponds to a specific elastic thickness value. Thereby the flexure curves are the inverse Fourier transform for a point load.

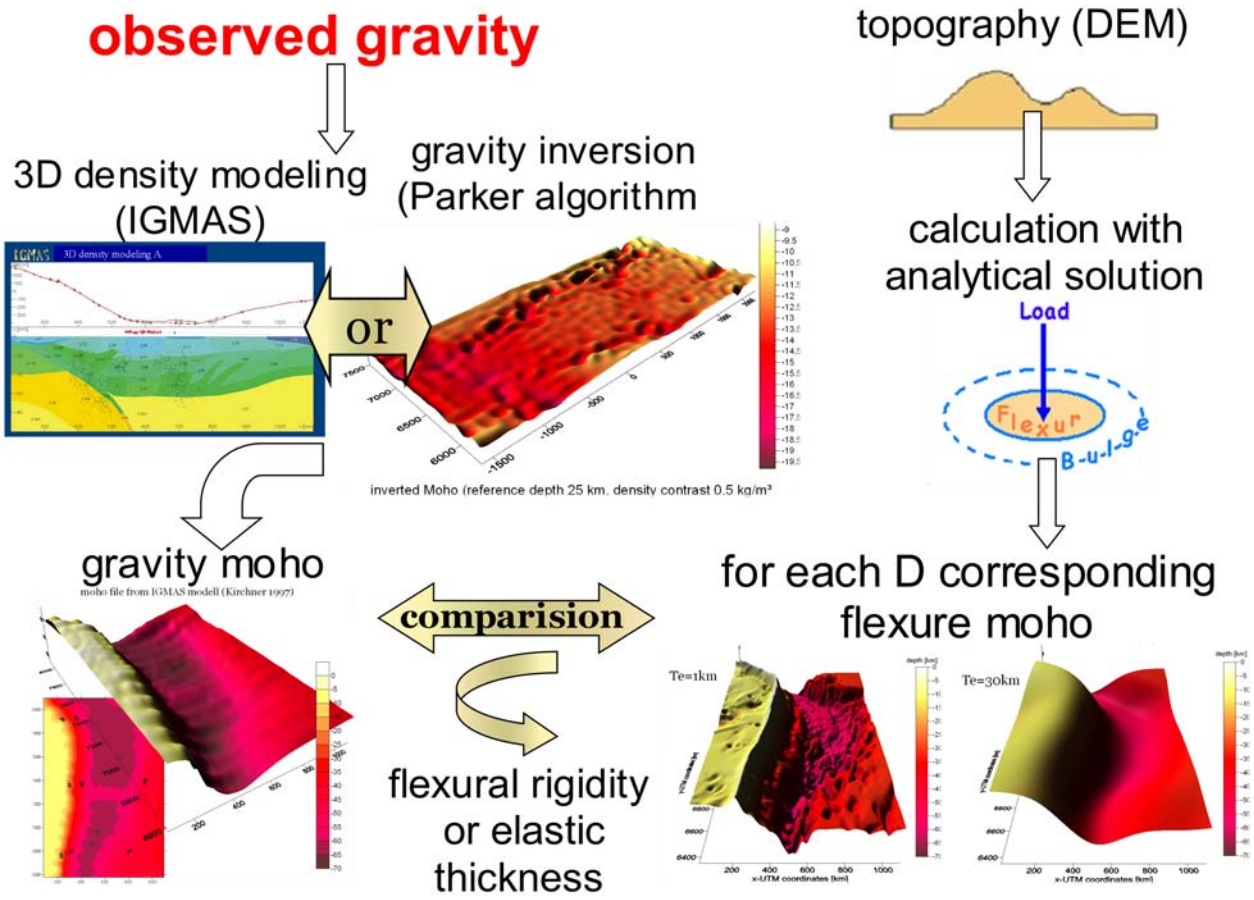

Figure 2.6.1) Shown is a float chart for estimation of elastic thickness or flexural rigidity, respectively, due to comparison of the gravity CMI and the flexure CMI.

The new analytical solution (see Chapter 2.3) was implemented in this computer software in order to calculate the flexure curves. In this software, as a further development called "coto", the analytical solution is multiplied with the grid distance dx, dy.

Additionally, the observed gravity values are used in order to derive a so-called "gravity CMI". This can be done by gravity inversion with the Parker algorithm (see Chapter 1.3) or by 3D density modeling with the software IGMAS (GÖTZE & SCHMIDT 1998).
In view of the fact that every flexure CMI corresponds to a specific value the elastic thickness/flexural rigidity distribution is indirectly obtained by comparison of the flexure CMI's with one reference gravity CMI. In order to compute this comparison I designed the software "gridrig".

2.6.2 Flexure curves and CMI

The computer software "coto" calculates the flexure curves with the analytical solution. The calculation time is 3-4 days (e.g. for a computer with 512MB Ram and a Pentium 4 CPU with 2,53 GHz) for each study area, described in Chapter 3. Thereby the function of the flexure curve is compound of the three analytical solutions (see Chapter 2.3). Then this flexure curve is convolved with the input grid (e.g. topography, load model, pseudo topography). The convolution of the flexure curve with the input load grid is done for each grid node within a radius of convolution. The result is a flexure CMI that corresponds to a specific elastic thickness value and a reference depth. Fig. 2.6.2 shows the flexure CMI for an input grid of a point load with $h = 1km$ and $T_e = 20km$.

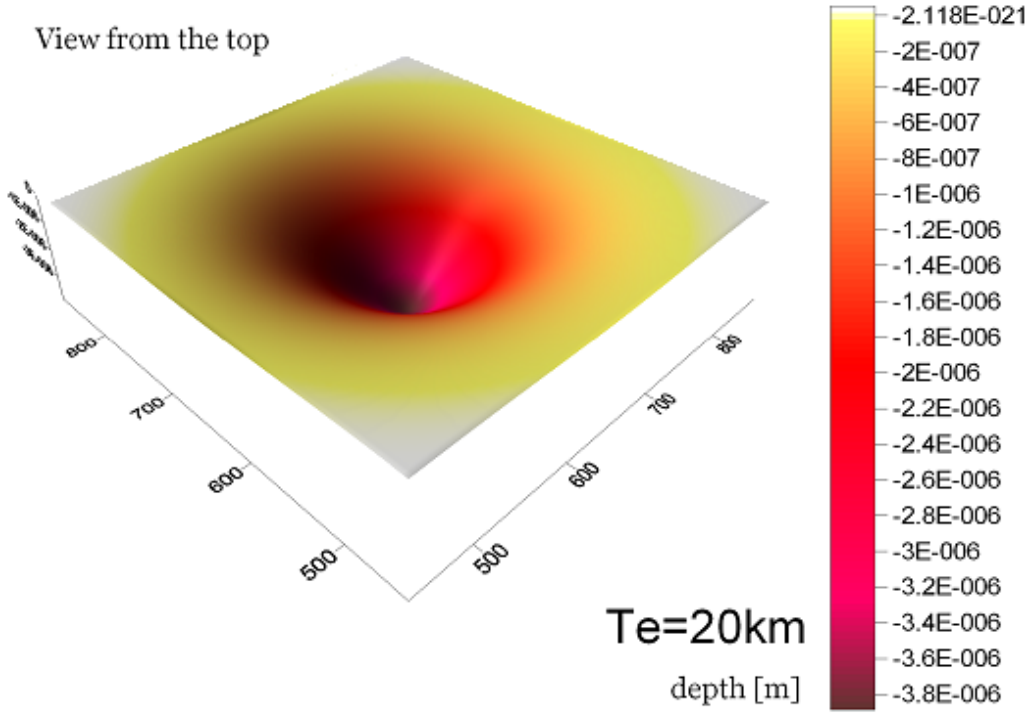

Figure 2.6.2) The CMI undulation for a point load is calculated with the elastic thickness value of $T_e = 20km$.

2.6.3 Radius of convolution

The computer software "coto" requires as input parameter the radius of convolution. The accuracy of the flexure CMI increases along with the radius of convolution. However,

regarding a rapidly increasing calculation time of the computer, it is important to choose the radius as small as possible but sufficiently large for producing significant results. For this reason I investigate the radius of convolution. Consequently, numerous flexure CMI's are calculated with different T_e values and a radius of convolution $R = 100;200;250km$. The flexure CMI's are compared with a reference CMI, computed with a radius of convolution of $R = 300km$. Fig. 2.6.3 shows the *RMS* values of the difference grids of the flexure CMI's and of the reference CMI.

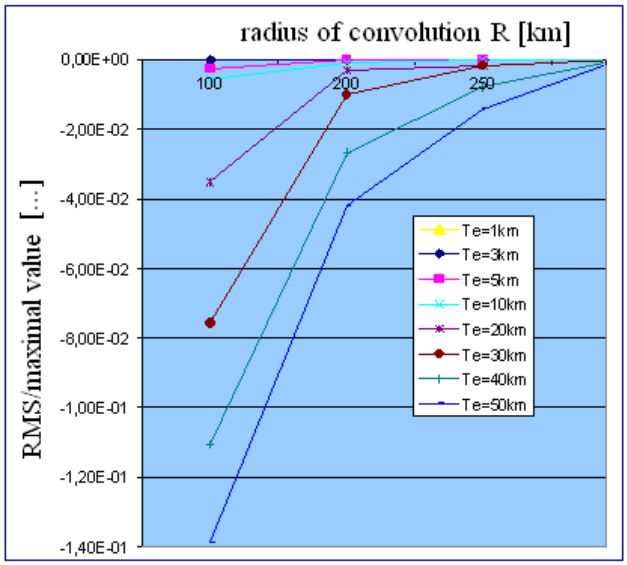

Figure 2.6.3) The RMS-value of the difference between reference CMI and flexure CMI is calculated for a point load as a function of radius of convolution.

Conclusively, the radius of convolution is dependent on the elastic thickness value. In view of this fact, I aim to use a function describing this dependency. Therefore the results are used from the investigation in Chapter 2.3 (see Eq. 2.3.13). Thereby the radius of convolution is equal to the distance of the first bulge. Various values for the radius of convolution are given in Table 2.6.1 for a density contrast at the CMI $\Delta\rho = 644kg/m^3$ and $\Delta\rho = 480kg/m^3$.

Elastic thickness $T_e[m]$	Radius of convolution $R = 3.88 \cdot \beta[m]$ for density contrast	
	$\Delta\rho = 644kg/m^3$	$\Delta\rho = 480kg/m^3$
1000	23751	25554
10000	133561	143701
20000	224622	241675
70000	574783	618418

Table 2.6.1) The radius of convolution was calculated with different $T_e[m]$ and density contrasts.

For calculating an elastic thickness value of $T_e = 1km$ a radius of convolution $R = 23km$ is required; for a higher elastic thickness value of $T_e = 70km$ a radius of convolution of $R = 574km$ is necessary using the density contrast $\Delta\rho = 644kg/m^3$. In the case the area of input load is to small , the result of the flexure CMI is not significant. The area of the load has to be chosen larger than the area of investigation, by the amount of the radius of convolution. The analytical solution leads to the advantage that the radius of convolution can directly be calculated as function of density contrast and elastic thickness.

2.6.4 Iterative estimation of elastic thickness

The computer software "coto" calculates one flexure CMI corresponding to one T_e value over the area of investigation with the radius of convolution. Hence, for $T_e = 1\ldots45km$, forty-five different flexure CMI's are computed. As example the area of the Pacific Ocean (Chapter 3.1) is chosen. With increasing of the elastic thickness value, the CMI undulation decreases (see Figure 2.6.4).

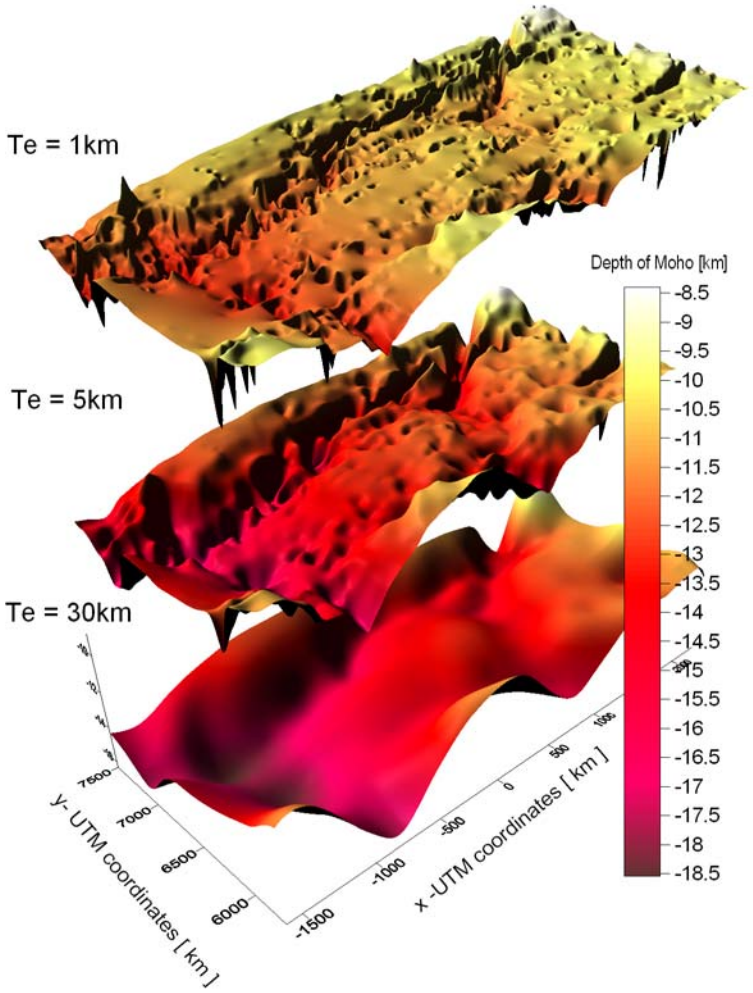

Fig 2.6.4) The flexure CMI was calculated for $T_e = 1;5;30km$. With increasing of T_e the CMI depth variations becomes smaller.

The difference of the flexure CMI is calculated with a reference CMI. Thereby the reference CMI is estimated by independent gravity observation. The software "gridrig" provides the best fitting flexure CMI (see float chart Fig. 2.6.5). The calculation time is 5-8 days (e.g. for a computer with 512MB Ram and a Pentium 4 CPU with 2,53 GHz).

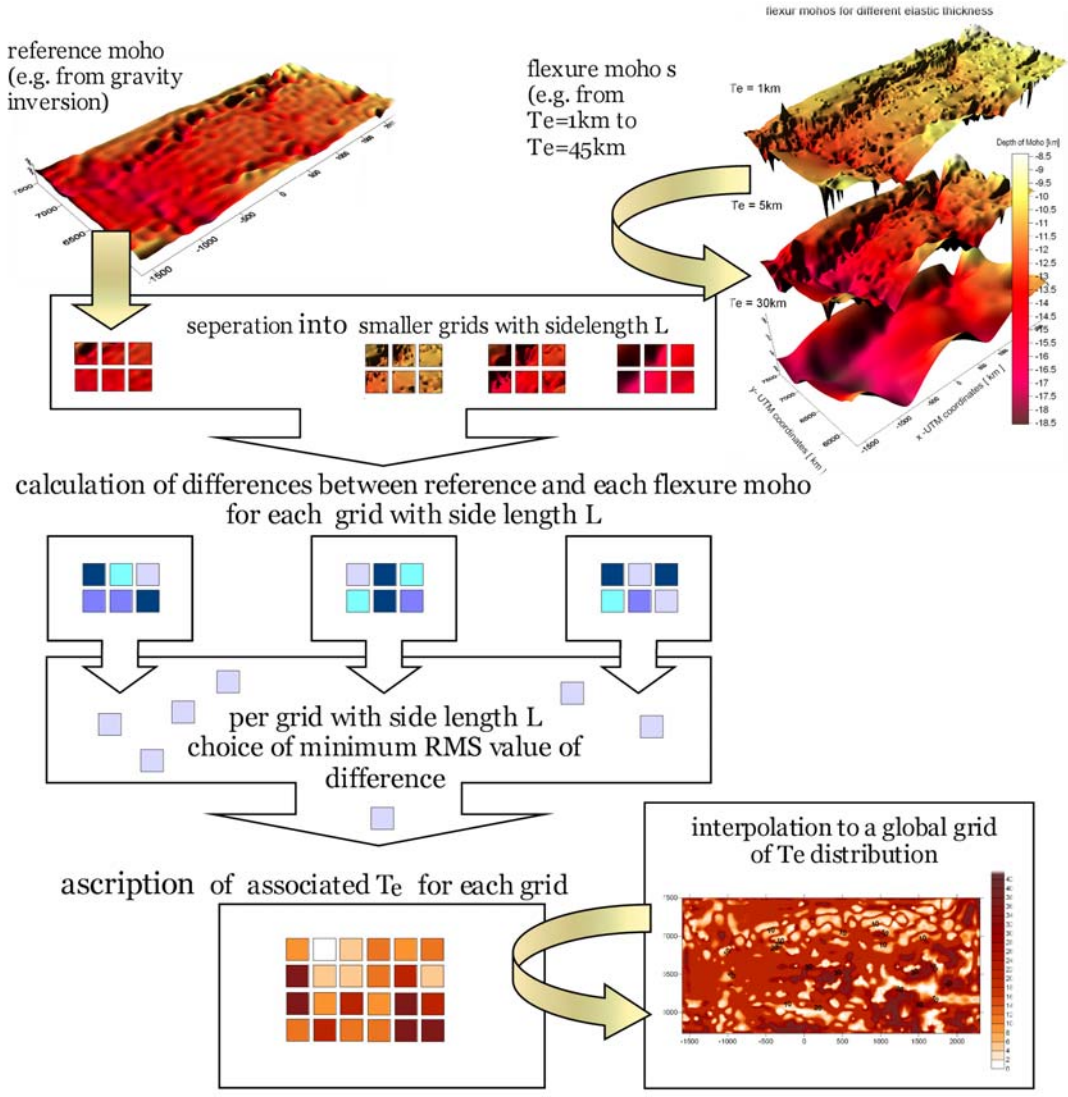

Figure 2.6.5) The float chart describes the software "gridrig", which calculates the difference grids and provides the elastic thickness distribution.

Given CMI and computed flexure CMI are divided in smaller areas with side length L (e.g. $L = 60km$). For each of these and each flexure CMI a difference grid is computed. The criterion of choice is the best fitting flexure CMI, accordingly the Root Mean Square (RMS value) is calculated. The grid with the smallest RMS provides the corresponding elastic thickness value. Thus a constant T_e value is given for each area. Each area has $x_{\min}$ / $x_{\max}$ and

y_{min} / y_{max} corner. The output grid of spatial distribution of elastic thickness or equivalent flexural rigidity is interpolated out of these data.

2.6.5 Elastic thickness distribution

The elastic thickness is calculated for a single area with side length L. The solution for a side length L , which converges to zero , is called “point solution”.

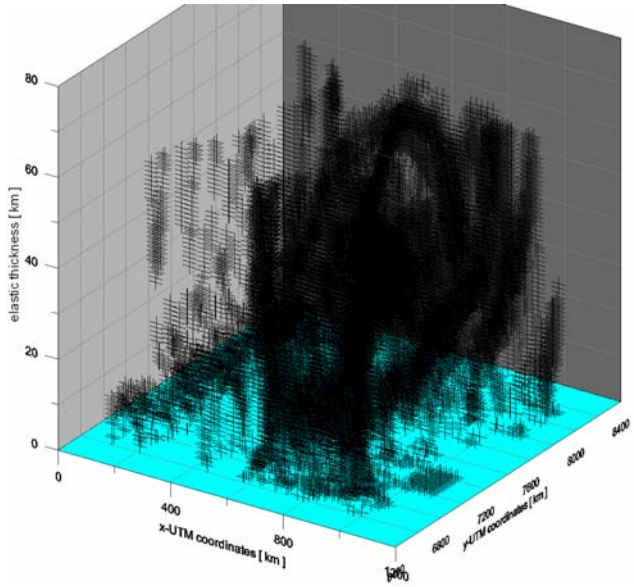

Figure 2.6.6) Shown are the results (black cross) of the solution in a point. As example the area of Central Andes was chosen.

In the following the solution of elastic thickness/flexural rigidity at a point is considered. I set as a criterion that the difference of the flexure and gravity CMI is smaller than $\Delta w \leq 650m$. The Figure 2.6.6 represents the results for the area of Central Andes as example (Chapter 3.2). For one point $p(x, y)$ a various number of elastic thickness values results. Obviously, the solution of the elastic thickness/flexural rigidity variation is equivocal. Hence, I obtain the difference between flexure and gravity CMI over a surface. In addition, a solution of T_e values for a surface intuitively is better understandable than for a point (PERS. COMM. GÖTZE). For this reason, it is essential to use the computer program “gridrig” (Fig. 2.6.3) for separating of the flexure CMI’s into smaller surfaces. This leads to the question, if the result of T_e is dependent on the grid size. Consequently, the results of T_e distribution will be compared for different side lengths L.

The T_e / D distribution (Figure 2.6.7) calculated with a grid size $L = 340km$ corresponds to an average value of the smaller grid size with $L = 60km$. The conclusion is, that the solution is independent on the grid size or side length L, respectively. Merely smaller grid sizes lead to higher resolutions of T_e distribution, but not to differing results.

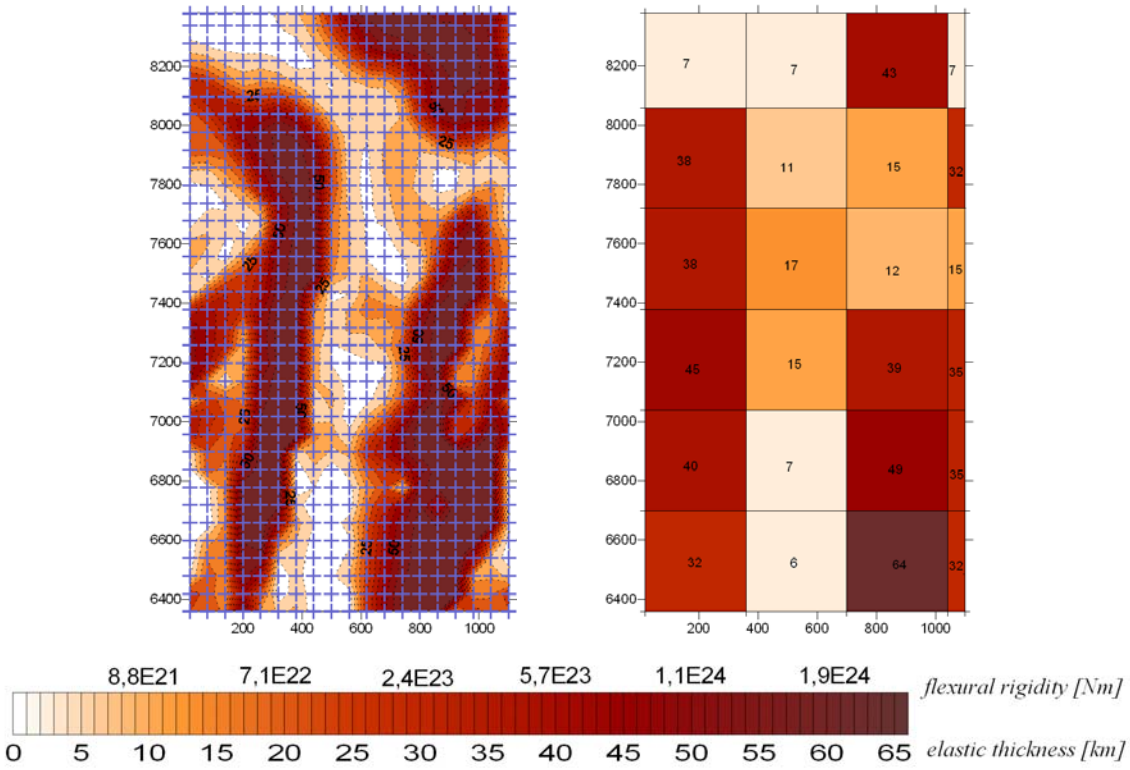

Figure 2.6.7) The results are compared for different grid size with $L = 340km$ and $L = 60km$. A smaller grid size leads to a higher resolution of T_e.

2.6.6 Reference depth

Because the solution for the T_e / D distribution is dependent on the reference depth (chapter 1.3, chapter 2.5) , the correct choice of this parameter is essential.

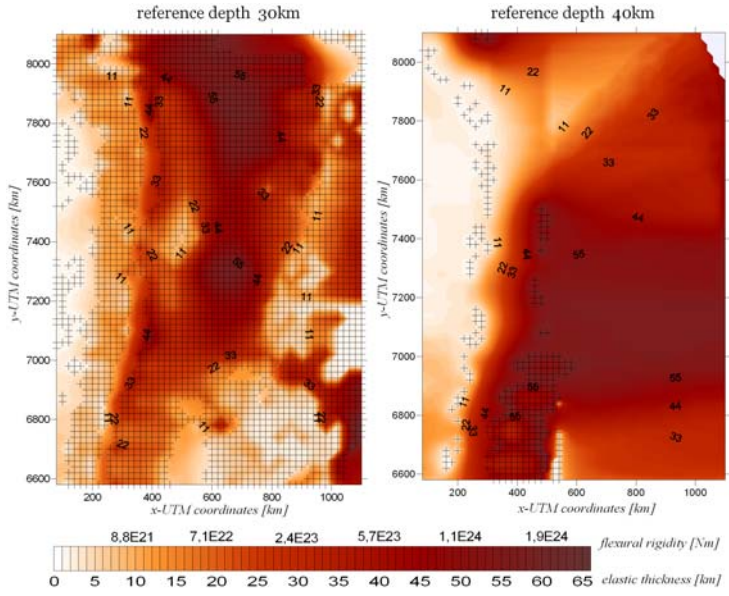

Figure 2.6.8) The results for different reference depth are compared with the criterion of difference value $\Delta w \leq 1km$ for a point solution (black crosses).

One possibility to prove the correct choice of the reference depth is the amount of results from the point solution. I set as criterion that the difference of the flexure and gravity CMI is $\Delta w \leq 1km$ and plot the numbers of results for different values of the reference depth (Fig. 2.6.8). As an example the area of Central Andes (see Chapter 3.2) is chosen, for a reference depth of $30km$ and $40km$. Additionally, the results of investigation of the reference depth are used (Chapter 2.5). Furthermore the reference depth can be estimated from independent information (e.g. seismic, seismology).

In Fig. 2.6.9 an example is shown for the area of the Pacific Ocean (see Chapter 3.1). The reference CMI is estimated by gravity inversion for a density contrast $\Delta\rho = 450kg/m^3$ and a reference depth of $30km$. The flexure CMI's are calculated for the same parameters but with different reference depths of $30km$ and $28km$. Obviously, the results for the elastic thickness variation are not strongly differing (see Fig. 2.6.9). The same features are recognized, but in the case of reference depth of $28km$ the resolution is lower. Furthermore, higher RMS values of difference are obtained for a reference depth $28km$.

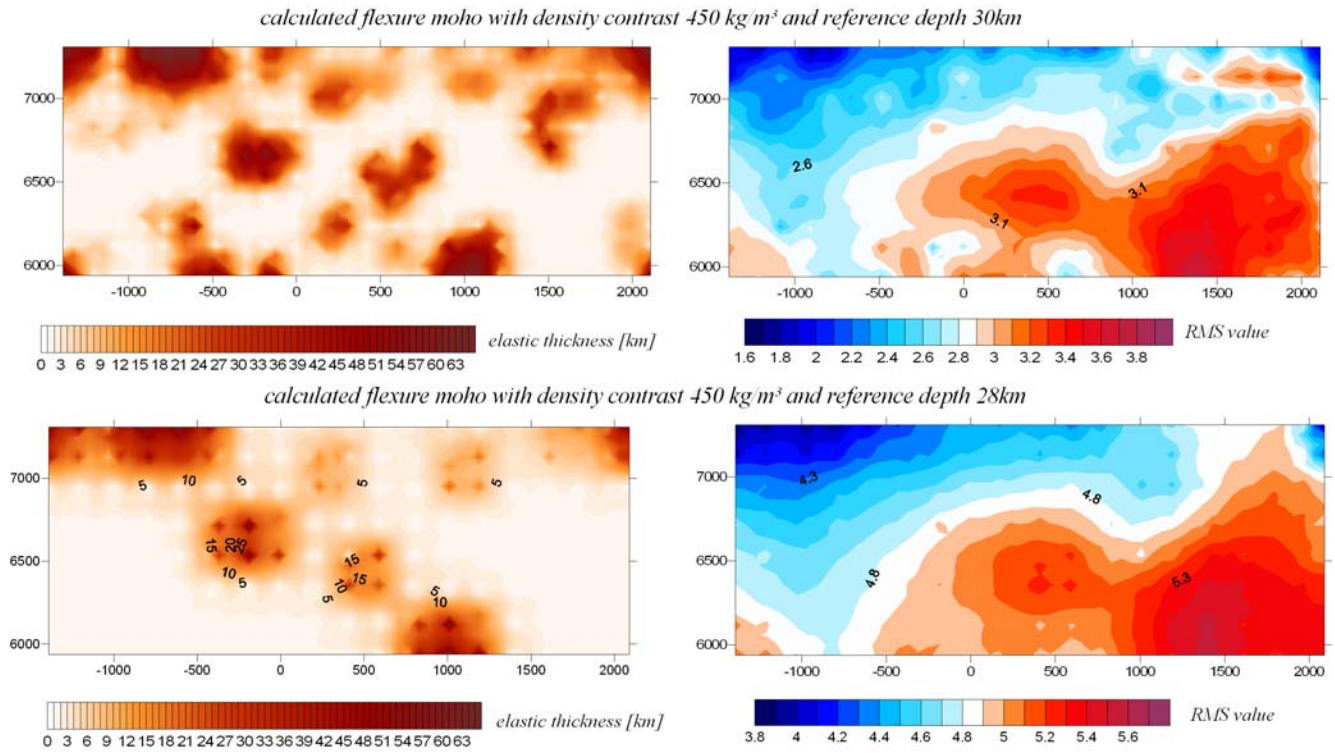

Figure 2.6.9) The results of elastic thickness variation and RMS values of the difference grid between flexure and gravity CMI are compared for different reference depths.

2.7 COMPARISON WITH FINITE ELEMENT MODELING

The finite element (short: FE) method is a powerful tool for the numerical simulation for example of mechanical problems and dynamic processes. An important advantage of the FE method is the flexibility to deal with complex geometries and boundary conditions. The variation of specific parameters and the determination of their relevance can easily be done. Another good advantage is that forward modeling is possible and the evolution of structures can be predicted.

A disadvantages of the FE method might be the way in which the problem is modeled: For example the approximations in the geometry or material properties, and the method of discretization, i.e. the number and type of elements used, both effect the accuracy of the final result (FAGAN 1992).

In this chapter the analytical solution is compared with the solution using FE modeling. Therefore various FE models were constructed by A. KELLNER (PERS. COMM.) with the program package EMRC-NISA and ABAQUS. The FE models are two dimensional, whereby the x direction is related to the x-coordinate and the z direction is associated to the depth. The displacement in z-direction corresponds to the deflection w for the analytical solution. The borders on the right and left side of the FE model are fixed ($\Delta x = \Delta z = 0$). This boundary condition is essential to avoid an escape of grid structures.

Due to the fact that I want to compare the FE solution with the analytical solution I have to make assumptions about the underlying foundation. The analytical solution is derived from the differential equation working for an elastic foundation (see Chapter 2.1).

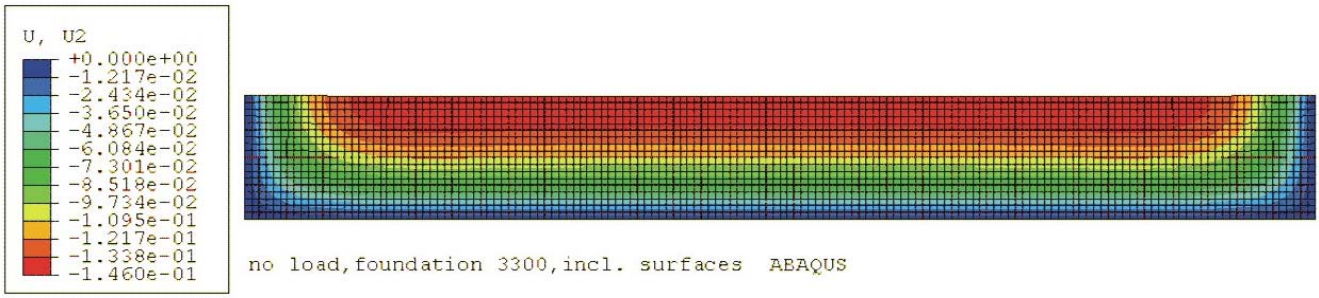

Figure 2.7.1) The displacement $[m]$ of the single elements of the FE model no.8 was calculated with gravity , but without load.

This concept of an elastic foundation is realized by springs locating at the bottom of the FE model with a spring constant k. Thereby k is calculated with $k = \rho_m \cdot g \cdot area$. The analytical solution and the FE solution is calculated for the same input parameters: density of crust $\rho_c = 2800 kg/m^3$, density of mantle $\rho_m = 3300 kg/m^3$, Young's Modulus $E = 10^{11} Pa$ and Poisson's ration $\nu = 0.25$. The displacement of the single elements of FE model no.8 is calculated with gravity but without a load (Figure 2.7.1).

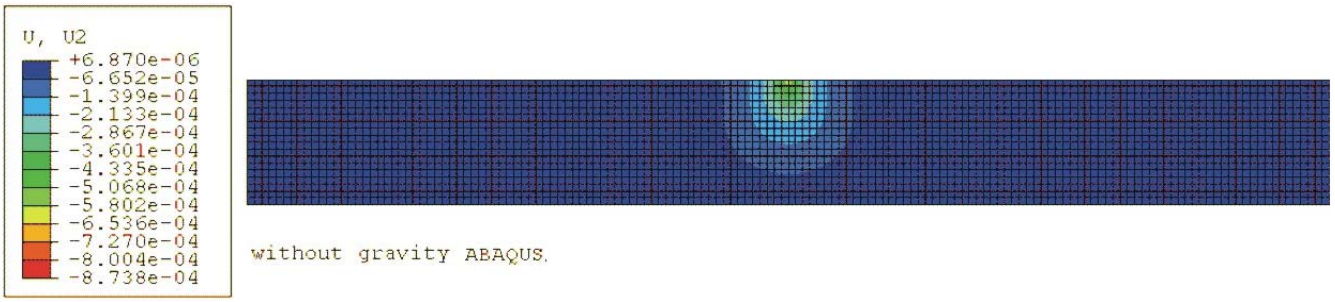

Figure 2.7.2) The displacement in $[m]$ of the single elements of the FE model no.15 was calculated for a point load and without gravity.

Obviously a deflection occurs only due to the presence of gravity. Unfortunately it was not possible to calculate a FE model with gravity and a point load (PERS. COMM. KELLNER). Therefore the deflection due to a load is estimated without gravity. As an example the model no.15 is chosen, calculated with the height of point load of $h = 1km$ (Fig. 2.7.2).

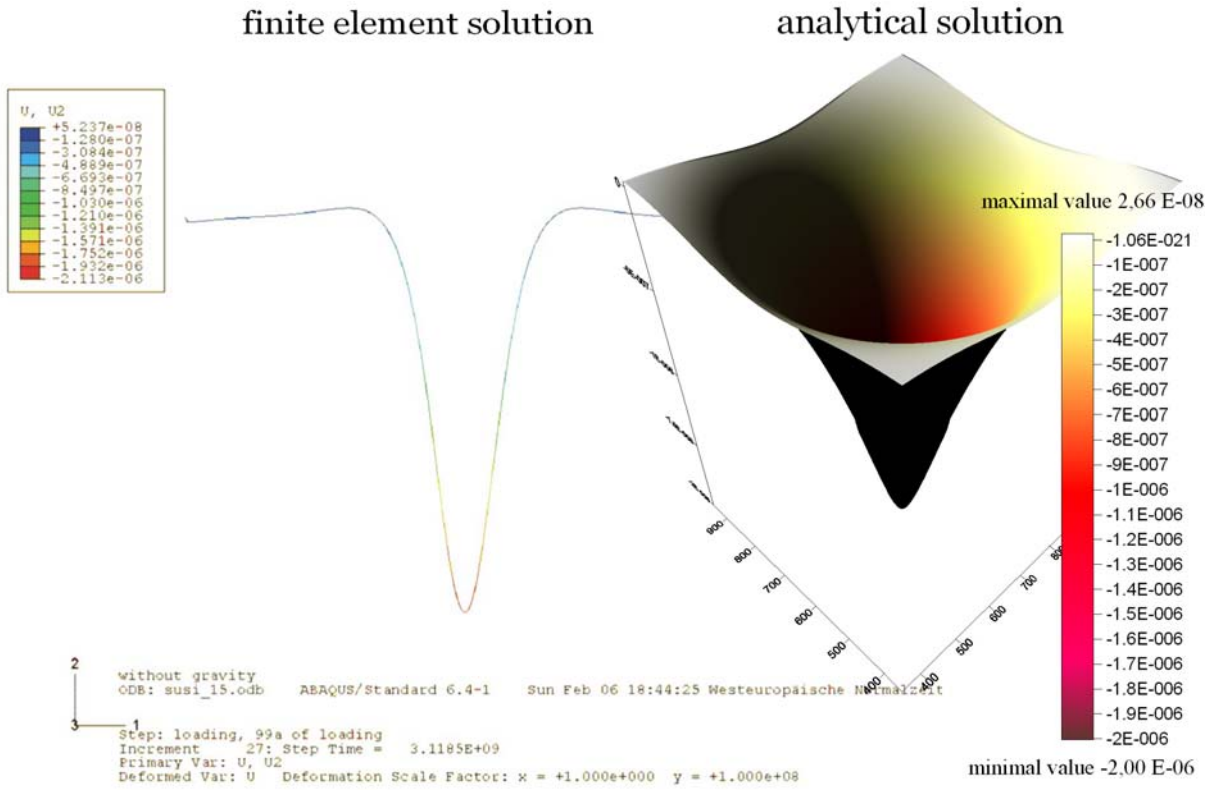

Figure 2.7.3) The displacement in $[m]$ of the bottom of the FE model No.15 is compared with the analytical solution for a point load.

Figure 2.7.3 shows the displacement of the bottom from the FE model No.15 , compared with the analytical solution computing with the same input parameters, except with gravity. The graph of the displacements shows the typical behavior of the flexure curves for a point load

(see Chapter 2.5). The solutions are comparable. The values for deflection move in the same range.

For a gravity value of $g = 10 m/s^2$ and an input grid of point load with height $h = 1 km$, and grid node distance $dx = dy = 5 km$ the depth values of the flexure CMI range between $-2.00 \cdot 10^{-6} m \leq w \leq 2.65 \cdot 10^{-8} m$. The displacement values for the FE solution range between $-2.11 \cdot 10^{-6} m \leq w \leq 5.24 \cdot 10^{-8} m$. In view of the fact that the deflection of the FE model is calculated in absence of gravity, I consider the flexure of the analytical solution for a small gravity value. For an assumed gravity value of $g = 1 m/s^2$ and an input grid of point load with height $h = 1 km$, the maximal depth value of the flexure CMI is $w_0 = -2.50 \cdot 10^{-6} m$ (see Fig. 2.7.4). Conclusively, the FE solution is reproducible by the analytical solution. Some uncertainties appear because the deflection of a point load topography is dependent on the grid distance of the input grid (discussed in Chapter 2.5). Therefore it would be useful to operate with a synthetic topography in the FE modeling. Additionally, an inaccuracy occurs due to the two dimensionality of the FE model. Therefore the point load would correspond to a line load (PERS. COMM. BRAITENBERG & KUKOWSKI). However, the analytical solution is comparable with the FE solution. The graph of deflection shows the same behavior as the analytical solution, for example the typical occurrence of the bulge (compare in Chapter 2.3 and 2.5).

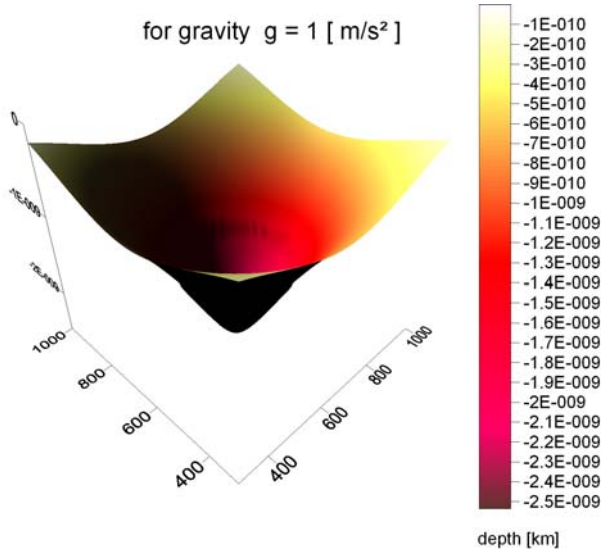

Figure 2.7.4) The deflection was calculated with the analytical solution for a point load and gravity $g = 1 m/s^2$.

2.7.1 Influence of input parameters

The following investigations were prepared in order to compare the principles of calculation of the deflection and to explore the influence of the density contrast and the change of Young's modulus, not focusing on the comparison of the exact values of deflection/displacement with the results of the analytical solution.

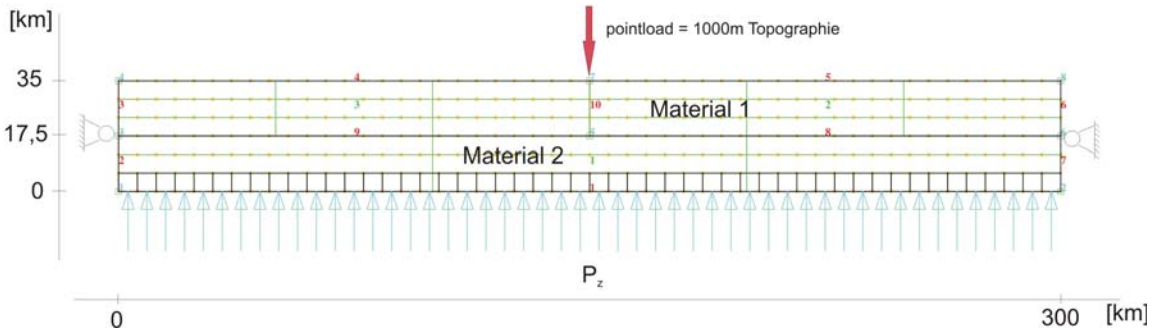

Figure 2.7.5) The settings of the FE models No.75, No. 79, No. 93 and No. 94.

The FE model consists of 2 layers. At the bottom acts a restoring force of $F = 1.06 \cdot 10^{-9} N$. The right and the left side of the model is fixed (Figure 2.7.5). The first layer consists of material 1 with a density of $\rho_1 = 2800 kg/m^3$; material 2 (of the second layer), has a density of $\rho_2 = 3300 kg/m^3$. Both materials have the same Young's modulus $E_1 = E_2 = 10^{11} Pa$ for the elastic case with gravity $g = 10 m/s^2$ the displacement is calculated. In the following the displacement of the elements are plotted for 7 node series corresponding to 7 different depths. Thereby series no.4 corresponds to the depth $z = 17.5 km$ for the undeformed FE-model (see Fig. 2.7.5) related to the interface between the 2 layers. The blue colored graph corresponds to the bottom of the FE model with a depth of $z = 35 km$. The displacement was calculated in the presence of gravity without a point load. As an example, FE model no. 75 is presented (Figure 2.7.6).

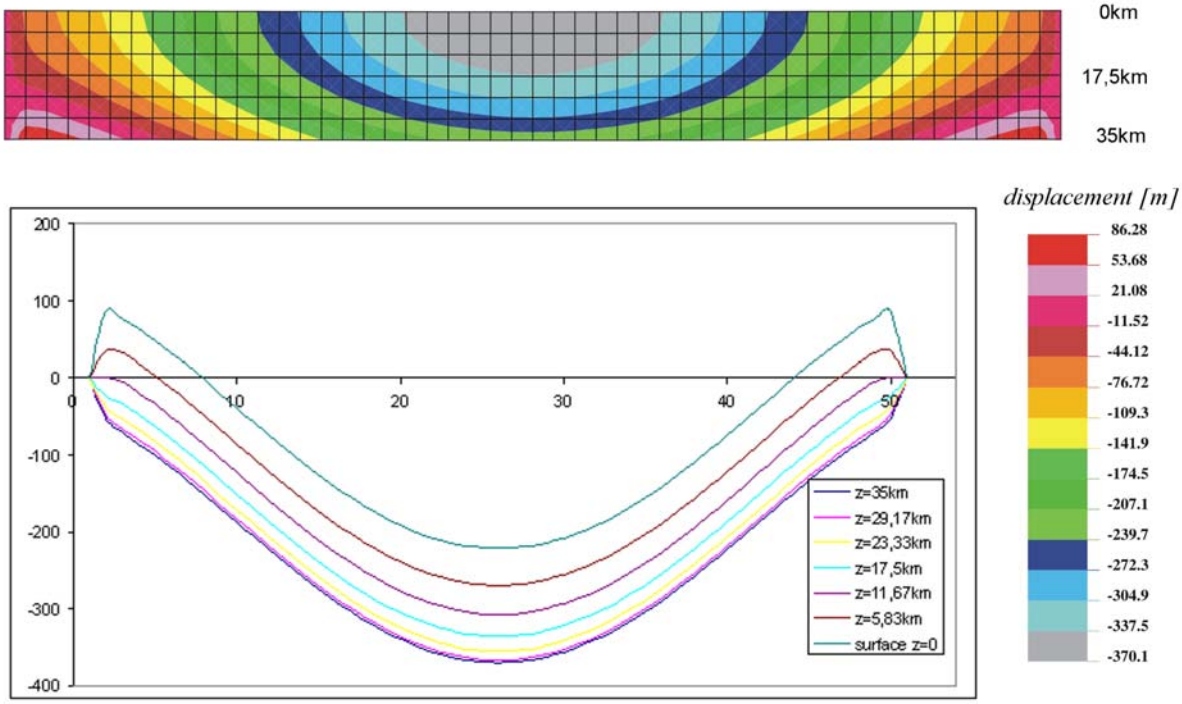

Figure 2.7.6) The displacement was calculated without a point load, the cyan line corresponds to the depth $z = 17.5 km$ and represents the border between the 2 layers. The blue graph corresponds to the base of the model.

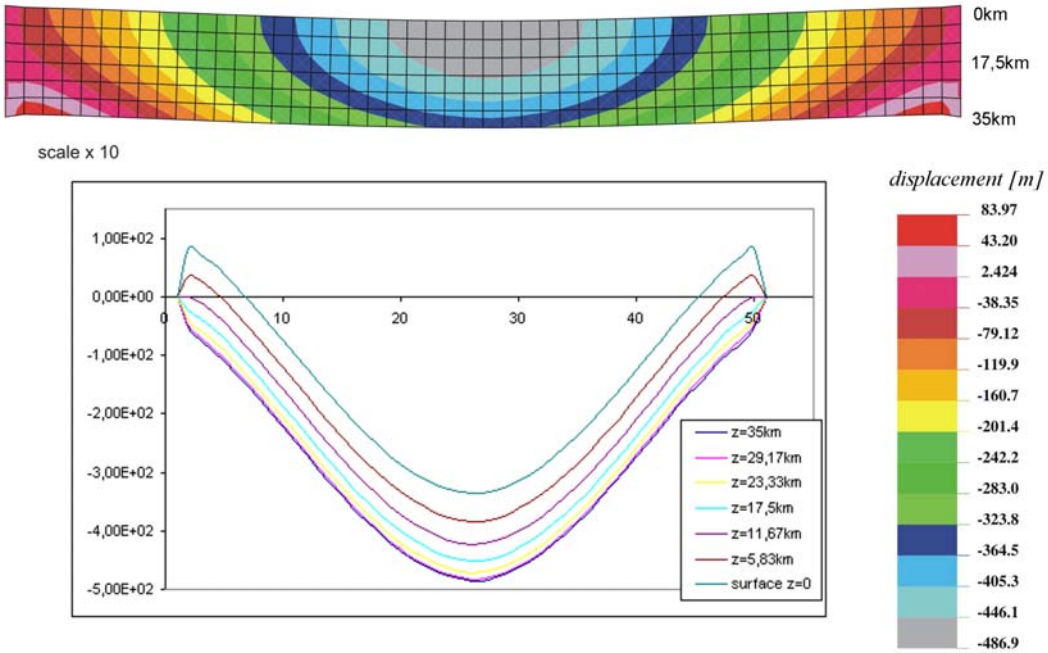

Figure 2.7.7) The displacement was calculated for a point load. The cyan colored line corresponds to the depth $z = 17.5km$ and the blue colored graph corresponds to the base of the model at the depth $z = 35km$.

Model no.79 is computed with the same input parameters. Additionally the displacement of the 7 node series is calculated for a point load with height $h = 1km$ (Fig. 2.7.7) in absence of the gravity. I use this model for comparison with the model no. 75. The difference between the FE model no. 79 and 75 is calculated. The resulting graph corresponds to a flexure due to a load (Fig. 2.7.8).

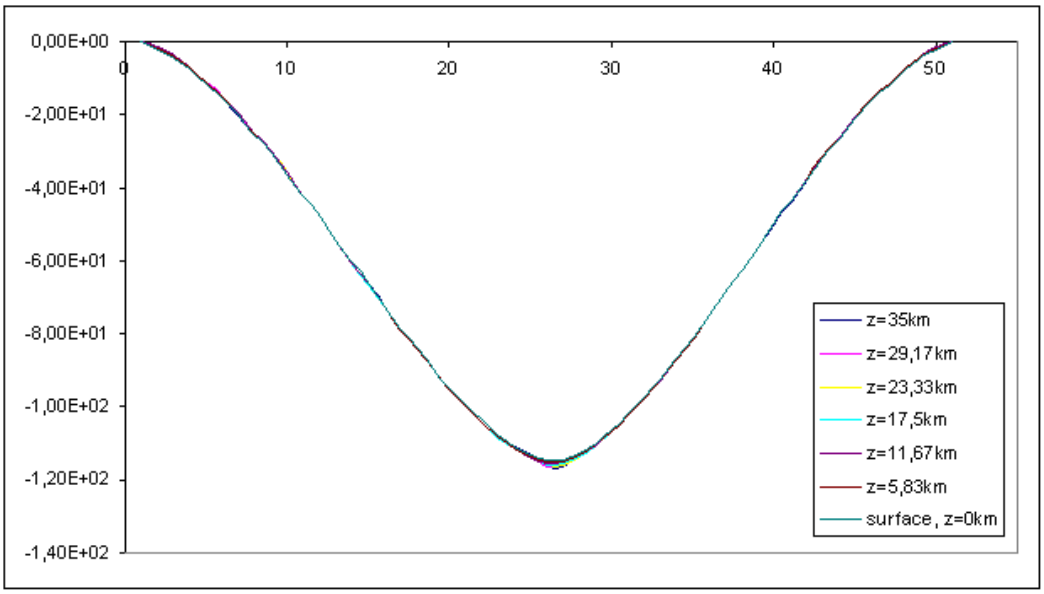

Figure 2.7.8) The difference in displacement of the elements is calculated of FE models no.79 and 75, corresponding to the flexure due to a point load with height of $h = 1km$.

Obviously, the flexure is almost equal for every node series (except in the point of the actual load). The flexure does not only occur at the interface between the 2 layers, but also at the base, where another restoring force is acting. I could interpret this flexure as flexure of a single layer model. Supposedly, I can summarize two layers of different densities to one layer if they have the same Young's modulus.

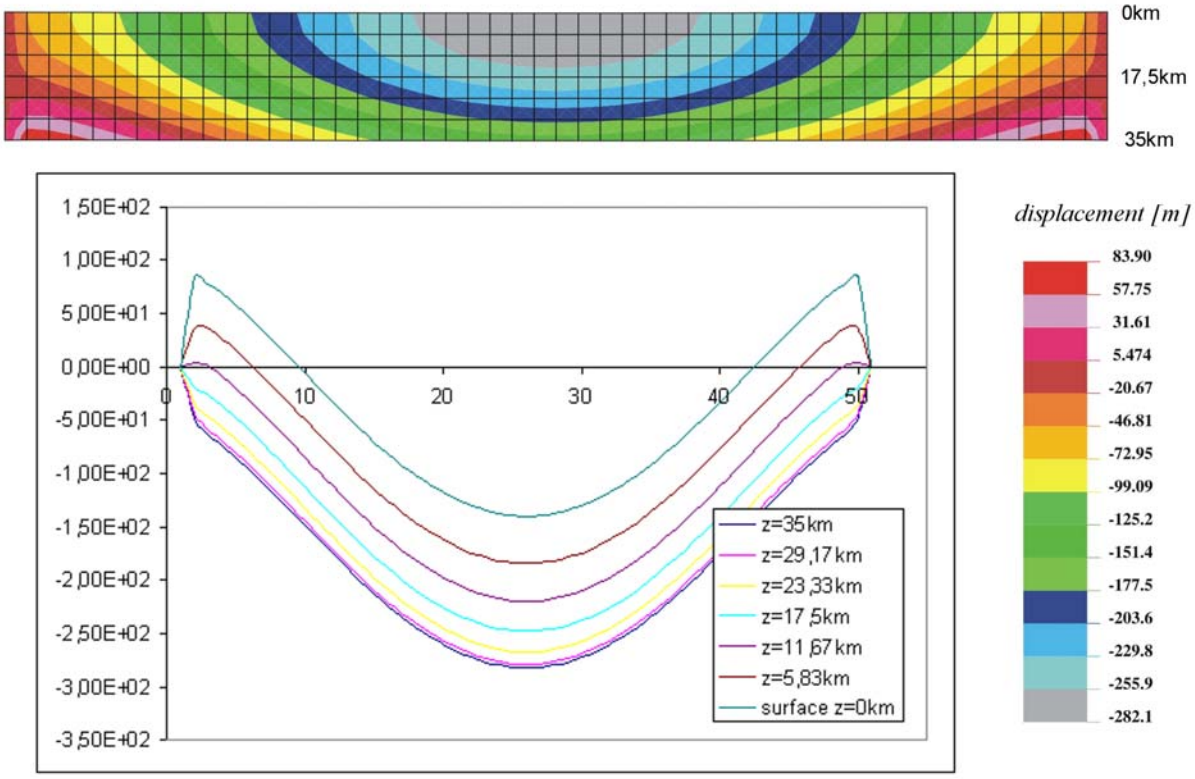

Figure 2.7.9) The displacement was calculated without a point load for a 1 layer model.

As evidence I consider a single layer model with the same settings (see Fig. 2.7.5); as example FE model no. 93 is chosen (Fig. 2.7.9). The displacement of the node series is calculated without a point load for a 1-layer model with a density $\rho_1 = 2800kg/m^3$. The curves of displacement show the same behavior as for the 2-layer model no.75, except that the amount of deflection differs.

The FE model no. 94 is computed with point load of height $h = 1km$ and with the same input parameter as model No. 93 (Fig. 2.7.10). Compared to the 2-layer model no. 79, the curves of displacement show the same behavior, but the amount of deflection differ. Therefore the amount of deflection is dependent from the density contrasts between the two layers.

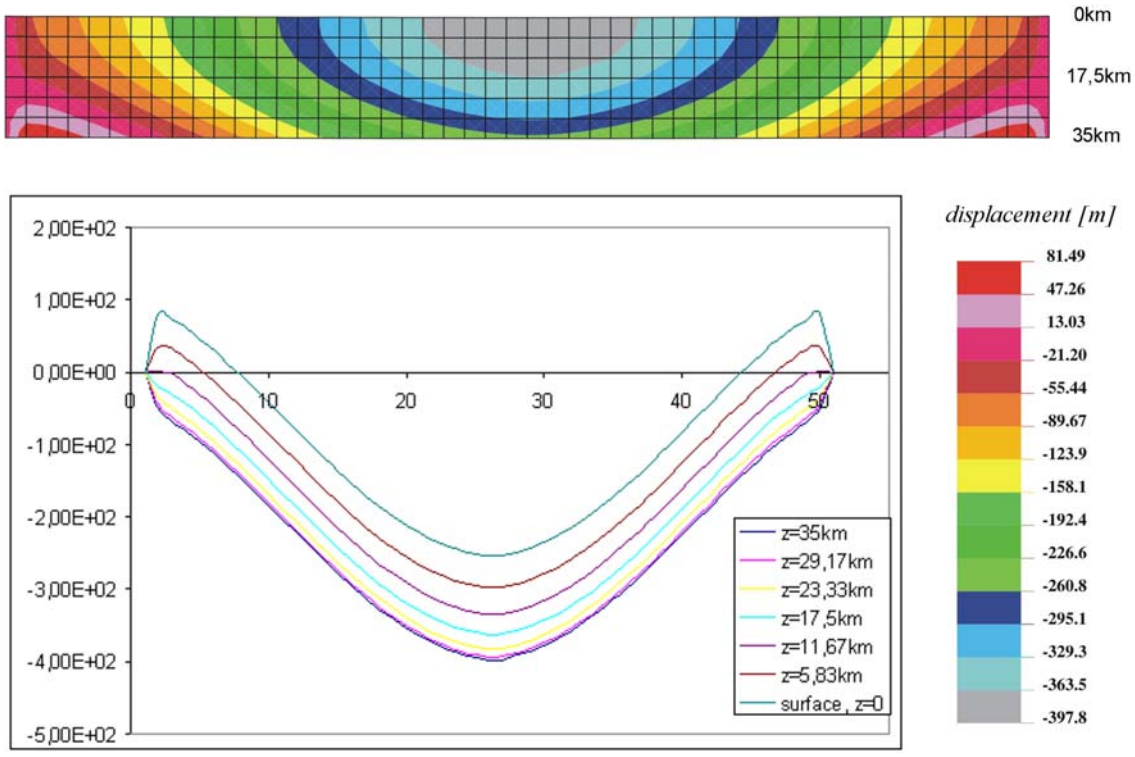

Figure 2.7.10) The displacement is calculated with a point load, for a 1-layer model.

However, considering the difference of displacement between model no. 93 and no. 94, the deflection due to a point load is obtained. The displacement is equivalent to the displacement of the 2-layer model (see Fig. 2.7.11).

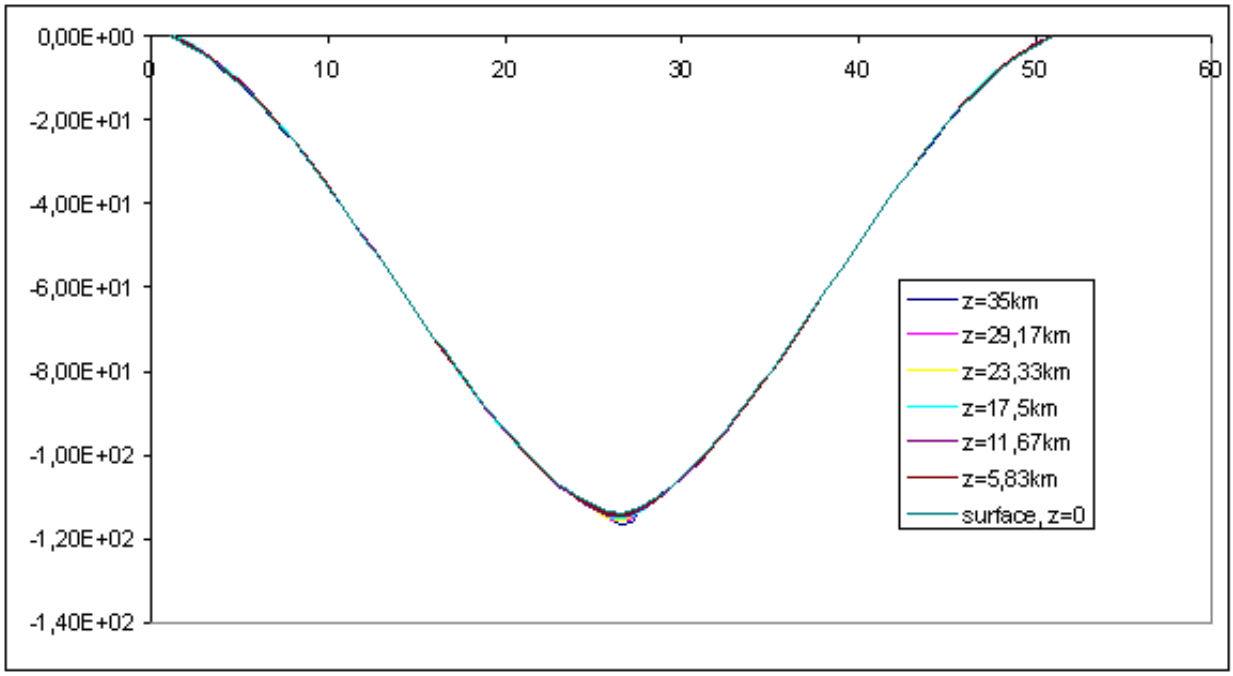

Figure 2.7.11) The difference in displacement for FE models No. 93 and 94 corresponds to the flexure due to a point load of height $h = 1km$.

Summarizing the results (Table 2.7.1) is concluded that the amount of deflection/displacement differs for a 1-layer or 2-layer model in dependence of the density. The difference between the displacements of the FE models calculated with and without load corresponds to the flexure due to a point load. The resulting graph is independent of the fact, if the calculation is done for a 1-layer or 2-layer model.

	name	load	max. displacement $w_0[m]$	difference $\Delta w_0[m]$
2 layer	model 75	no	-370.1	-119
	model 79	yes	-486.9	
1 layer	model 93	no	-282.1	-119
	model 94	yes	397.1	

Table 2.7.1) The results of FE-modeling are summarized for the models, which consists of 1 and 2 layer, respectively.

Supposedly, it is sufficient to handle the layers with different densities like one single plate with one thickness and an average density. The resulting deformation is comparable with the deformation occurring for a single plate (1 layer), if the Young's modulus of the 2 layers with different densities is equal.

Therefore I will investigate the deformation for a variation of Young's modulus. The following FE-models have the same settings; but the material 1 for the first layer has a Young's modulus $E_1 = 10^{11} Pa$ and the material 2 has $E_2 = 10^{13} Pa$. The calculation is done without gravity. In the FE model no. 44 the displacement is calculated with a force $F = 10^{10} N$, instead of a point load. In contrast to the previous investigations is the deformation of a 2-layer model not comparable with the deformation of a single plate (1-layer model), if the Young's modulus changes (Fig. 2.7.12).

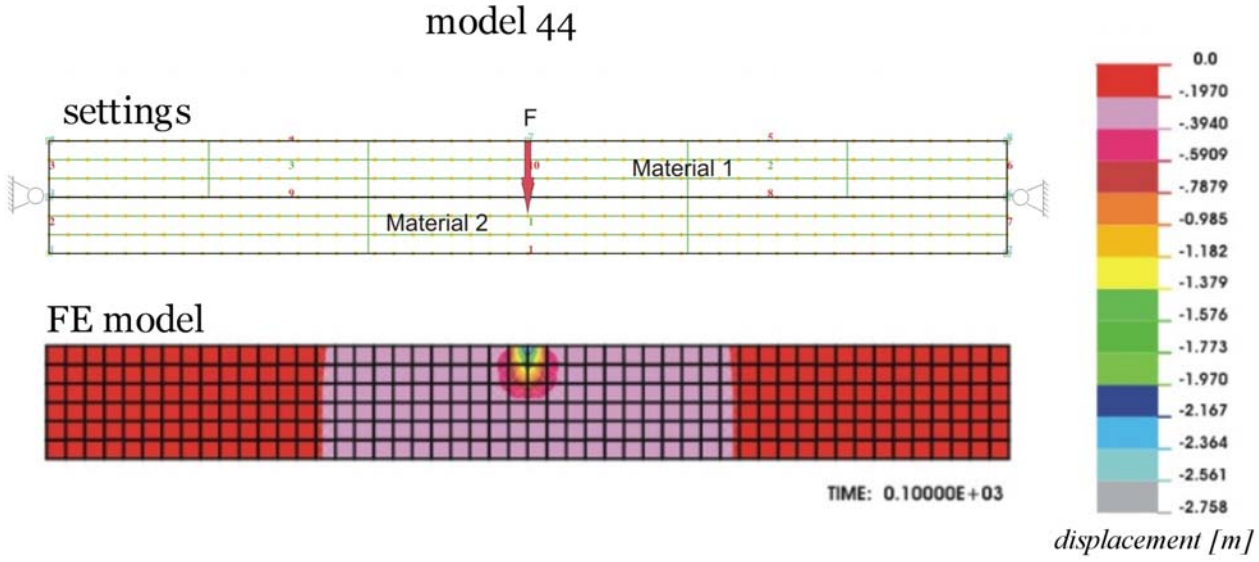

Figure 2.7.12) The displacement of the elements from FE models No. 44 corresponds to the flexure due to a force.

At the interface between the 2 layers the form of the flexure is changing. In view of the larger Young's modulus of the second layer ($E_2 > E_1$) decrease the amount of deflection or displacement, respectively.

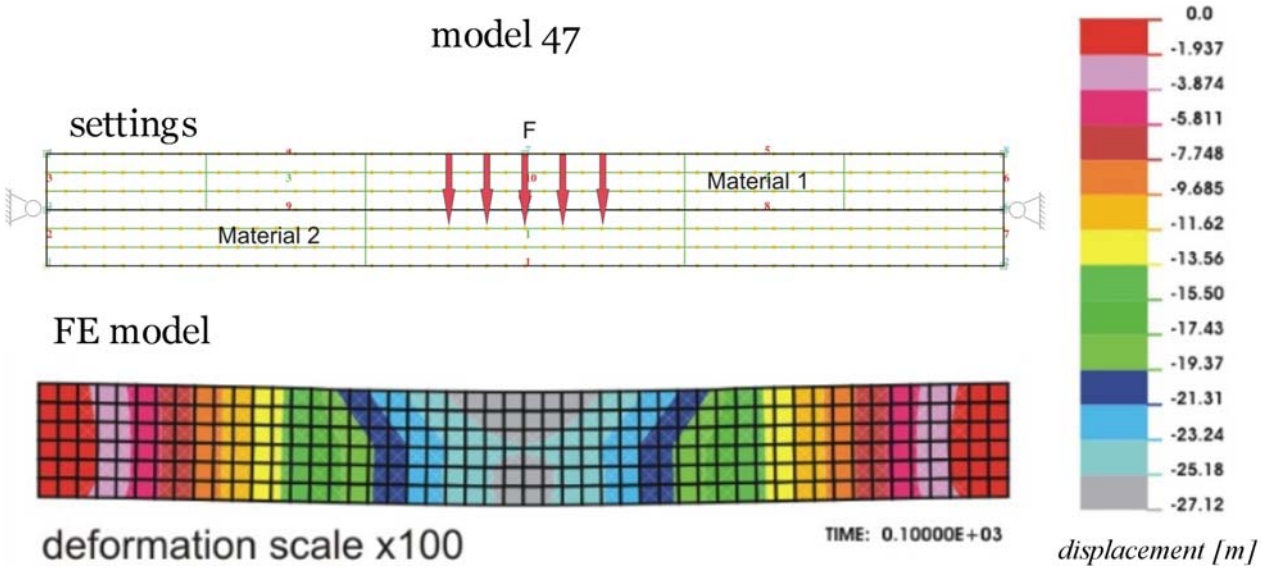

Figure 2.7.13) The displacement of the elements from FE models No. 47 was calculated with 5 forces of equal amount.

The following FE models are calculated with the same input parameters, but with different forces varying in form and amount. The displacement of the FE model No.47 is calculated with 5 forces with an amount of $F = 10^{10}\,N$ (Figure 2.7.13). At the interface between the 2 layers a change in the amount of deflection/displacement is obtained, caused by the increase in Young's modulus of the second layer.

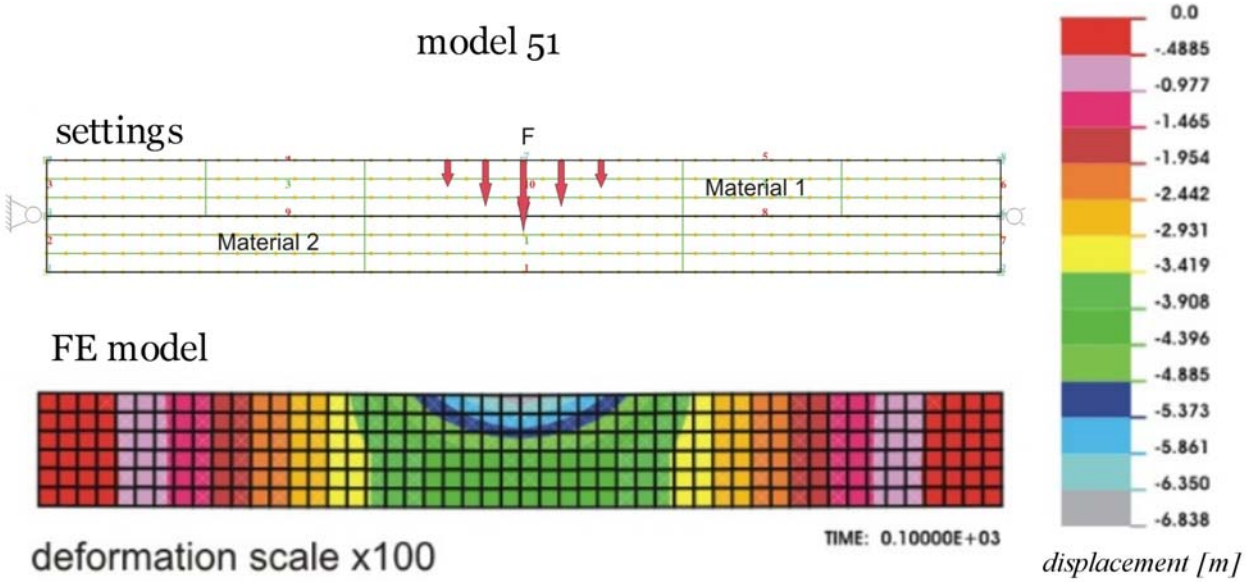

Figure 2.7.14) The displacement of the elements from FE models No. 51 was computed for 5 different forces.

In FE-model No.51 the displacements is calculated with the same input parameters (compared to model No.47), but with 5 forces of different amount ranging from $F_{max} = 10^{10}\,N$ to $F_{min} = 10^{8}\,N$ (Fig. 2.7.14). A superposition of the 5 forces is obtained. At the interface between the two layers a decrease in the deflection is obtained caused by the larger E modulus of the second layer.

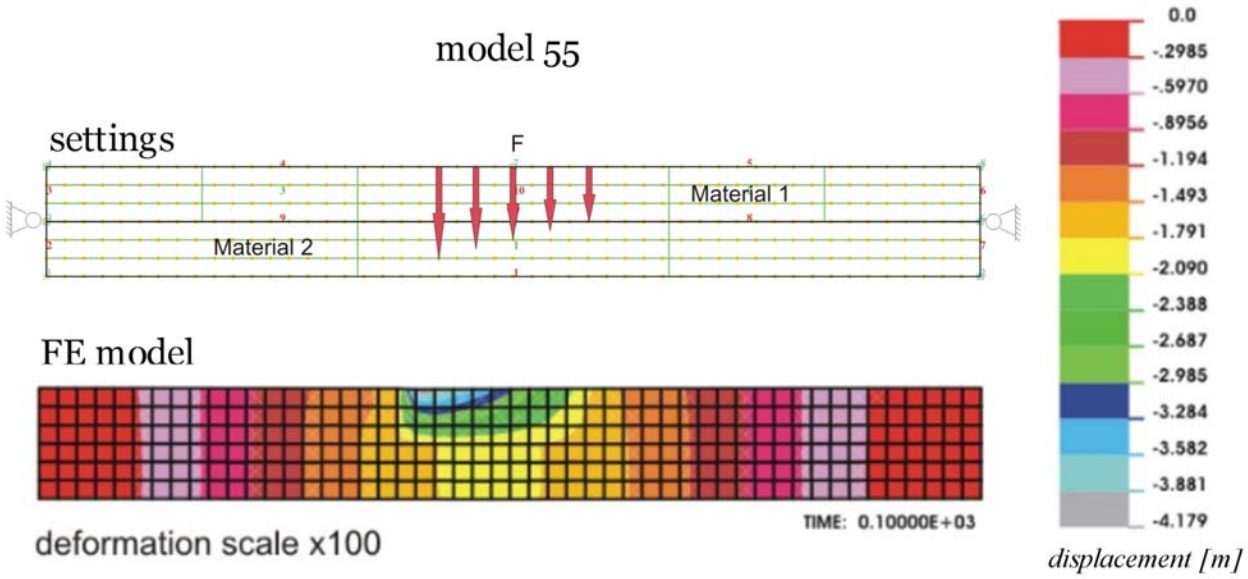

Figure 2.7.15) The displacement for FE models No. 55 was computed for 5 different forces.

FE model No. 55 illustrates the propagation of the „shape“ of the forces in the displacement (Fig. 2.7.15): The maximal deflection occurs in the first layer where the maximal force is acting. In the second layer the deflection decrease due to the larger Young's modulus of the material 2. The value for the maximal deflection of the first layer moves in the same number range as model No. 44. The results for the maximum displacements of the four FE models are summarized in Table 2.7.2.

name	F or $F_{max} / F_{min} [N]$	max. displacement $w_0 [m]$
model 44	-10^{10}	-2.75
model 47	-10^{10}	-27.11
model 51	$-10^{10} / -10^{8}$	-6.84
model 55	middle $-10^{10} / -10^{8}$	-4.18

Table 2.7.2) The values of maximum displacements are summarized for different FE models.

2.7.2 Conclusion

The results of the FE modeling lead to conclusions concerning the calculation of the flexure of a thin plate with the analytical solution. It is assumed that the first layer with a density of $\rho_1 = 2800 kg/m^3$ represents the crust and the second layer with a density of $\rho_2 = 3300 kg/m^3$ the mantle and a superposition of forces. Furthermore I can conclude that the propagation of the deflection between the crust and mantle interface is dependent from the Young's modulus. The change of Young's modulus drives the form of deformation.

The question, if the deflection of the CMI or the deflection of the lithosphere/asthenosphere boundary (short: LAB) is considered, dependents from the depth at which the Young's modulus changes. I can interpret the general concept of calculation of a flexure, that with the reference depth the calculated flexure-surface is shifted at the depth where the change of Young's modulus is assumed. Therefore the calculated flexure is valid at one hand for the CMI and at the other hand for the LAB. If the Young's modulus of the crust and upper mantle is equal, than the crust and upper mantle deforms like one single plate. The density contrast drives only the amount of deflection or displacement, respectively.

Because of the complex procedure required for a FE modeling, further investigation are not made. Especially the consideration of all ideas is unfortunately not possible in the frame of this thesis.